

This is an Open Access document downloaded from ORCA, Cardiff University's institutional repository:<https://orca.cardiff.ac.uk/id/eprint/127684/>

This is the author's version of a work that was submitted to / accepted for publication.

Citation for final published version:

Hodge, Michael , Biggs, Juliet, Fagereng, Ake , Mdala, H., Wedmore, L. and Williams, Jack 2020. Evidence from high resolution topography for multiple earthquakes on high slip-to-length fault scarps: the Bilila-Mtakataka fault, Malawi. *Tectonics* 39 (2) , e2019TC005933. 10.1029/2019TC005933

Publishers page: <http://dx.doi.org/10.1029/2019TC005933>

Please note:

Changes made as a result of publishing processes such as copy-editing, formatting and page numbers may not be reflected in this version. For the definitive version of this publication, please refer to the published source. You are advised to consult the publisher's version if you wish to cite this paper.

This version is being made available in accordance with publisher policies. See <http://orca.cf.ac.uk/policies.html> for usage policies. Copyright and moral rights for publications made available in ORCA are retained by the copyright holders.



1 **Evidence from high resolution topography for multiple**
2 **earthquakes on high slip-to-length fault scarps: the**
3 **Bilila-Mtakataka fault, Malawi**

4 **M. Hodge¹, J. Biggs², Å. Fagereng¹, H. Mdala³, L. Wedmore², J. Williams¹**

5 ¹School of Earth and Ocean, Cardiff University, UK

6 ²School of Earth Sciences, University of Bristol, UK

7 ³Geological Survey Department, Malawi

8 **Key Points:**

- 9
- 10 • We use satellite topography and a numerical model to analyse normal fault scarps
11 and knickpoints potentially reflecting multiple earthquakes
 - 12 • The Bilila-Mtakataka fault, Malawi, shows evidence for at least two previous rup-
13 tures with up to 10-12 m of vertical offset each.
 - 14 • The degradation of the scarps suggests a diffusion age of 48 ± 25 m² correspond-
ing to 6.4 ± 4.0 kyr since formation.

Corresponding author: Juliet Biggs, juliet.biggs@bristol.ac.uk

15 **Abstract**

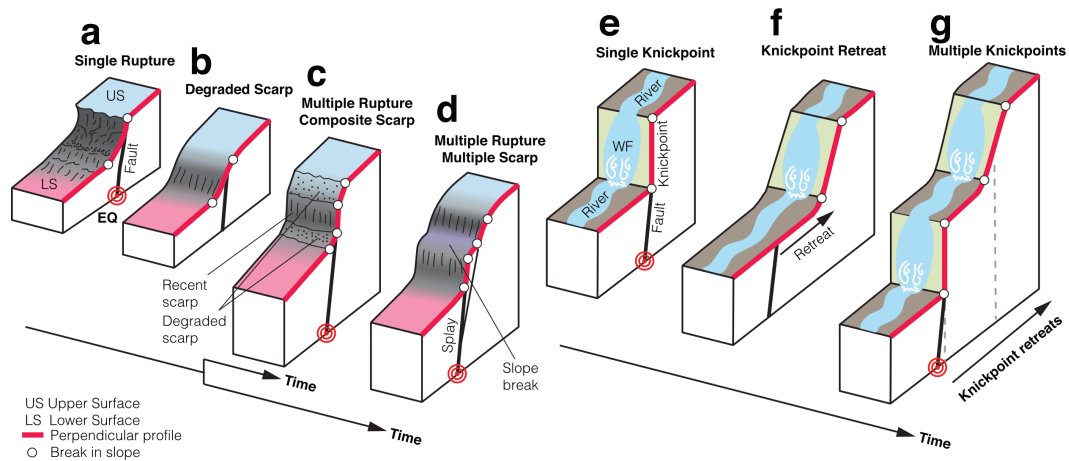
16 Geomorphological features such as fault scarps and stream knickpoints are indi-
 17 cators of recent fault activity. Determining whether these features formed during a sin-
 18 gular earthquake or over multiple earthquakes cycles has important implications for the
 19 interpretation of the size and frequency of past events. Here, we focus on the Bilila-Mtakataka
 20 fault, Malawi, where the 20 m high fault scarps exceed the height expected from a sin-
 21 gular earthquake rupture. We use a high resolution digital elevation model (< 1 m) to iden-
 22 tify complexity in the fault scarp and knickpoints in river profiles. Of 39 selected scarp
 23 profiles, 20 showed evidence of either multi-scarps or composite scarps and of the seven
 24 selected river and stream profiles, five showed evidence for multiple knickpoints. A near
 25 uniform distribution of vertical offsets on the sub-scarps suggests they were formed by
 26 separate earthquakes. These independent methods agree that at least two earthquakes
 27 have occurred with an average vertical offset per event of 10 and 12 m. This contrasts
 28 earlier studies which proposed that this scarp formed during a single event, and demon-
 29 strates the importance of high-resolution topographic data for understanding tectonic
 30 geomorphology. We use a one-dimensional diffusion model of scarp degradation to demon-
 31 strate how fault splays form multi-scarps and estimate the diffusion age κt of the Bilila-
 32 Mtakataka fault scarp to be $48 \pm 25\text{m}^2$, corresponding to 6400 ± 4000 years since for-
 33 mation. We calculate that a continuous rupture would equate to a $M_W 7.8 \pm 0.3$ earth-
 34 quake, greater than the largest seismic event previously recorded in East Africa.

35 **1 Introduction**

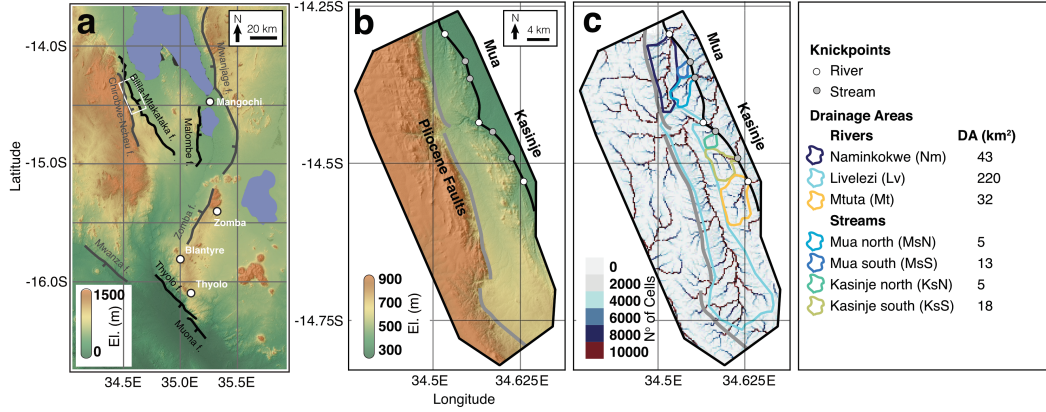
36 Historical and instrumental catalogues alone provide a short and incomplete record
 37 of past earthquakes (e.g. McCalpin, 2009; Hodge et al., 2015), and devastating earth-
 38 quakes may occur on faults that have no historical earthquake activity (e.g. 2003 $M_W 6.6$
 39 Bam earthquake in Iran; Fu et al., 2004). By investigating fault-generated landforms such
 40 as fault scarps, an assessment of the earthquake and rupture history along a fault, and
 41 the probability and hazard of future earthquakes, can be made (e.g. Wallace, 1977; Duffy
 42 et al., 2014; Zhang et al., 1991; Bucknam & Anderson, 1979; Zielke et al., 2015; Nash,
 43 1980; Hanks et al., 1984; Andrews & Hanks, 1985). Paleoseismological trenching can pro-
 44 vide information about timing and magnitude of prehistoric earthquakes (e.g. Schwartz
 45 & Coppersmith, 1984; Michetti & Brunamonte, 1996; Palyvos et al., 2005), but trench-
 46 ing requires particular geomorphic conditions and is limited by site accessibility.

47 Estimates of the displacement and age of earthquake ruptures can be made from
 48 geomorphical analyses of fault scarps and river channels (e.g. Bucknam & Anderson, 1979;
 49 Avouac, 1993). The latest generation of satellite-derived Digital Elevation Models (DEMs)
 50 have sufficient resolution for these estimates to be made remotely (Figure 1). In cases
 51 where there are subtle changes in morphology, such as slope breaks within the fault scarp,
 52 the existence of multiple ruptures can be analysed (Wallace, 1980, 1984) for compari-
 53 son with other paleoseismological records (Ewiak et al., 2015). Furthermore, along-strike
 54 comparisons, which are not possible with point sampling methods such as trenching, can
 55 be used to analyse the structural evolution of the fault (e.g. Perrin et al., 2016a; Crone
 56 & Haller, 1991; Manighetti et al., 2005; Hodge et al., 2018b, 2019). Rivers and streams
 57 crossing fault scarps may also preserve indicators of past earthquakes in the form of ver-
 58 tical steps - called knickpoints - in an otherwise convex and smooth longitudinal profile
 59 (e.g. Ouchi, 1985; Holbrook & Schumm, 1999; Wei et al., 2015; Burbank & Anderson,
 60 2011). These can be used to identify active fault traces in regions with complex topog-
 61 raphy (Litchfield et al., 2003), and for paleoseismological analysis (Wei et al., 2015; Ewiak
 62 et al., 2015).

75 In this study, we investigate whether indicators of multiple ruptures exist along two
 76 major structural segments of the Malawi Rift's Bilila-Mtakataka fault (BMF). Earlier
 77 studies suggested that the scarp may reflect a single earthquake that ruptured the whole



63 **Figure 1.** Various geomorphic indicators of multiple ruptures in an idealised system assuming
 64 no lithological contrasts or bedrock fabric. a) A single rupture scarp, where the upper original
 65 surface (US) and lower original surface (LS) are separated by a scarp formed of a steep free face,
 66 and wash and debris faces. The elevation profile (red line) shows two prominent changes in slope
 67 marked by breaks in slope (white circles). b) A degraded scarp. Erosion and deposition of mate-
 68 rial smooths the scarp surface. Following another surface rupture, either: c) A composite scarp
 69 forms, where the most recent rupture is indicated by a steeper slope on the scarp surface; or d)
 70 A multi-scarp forms where individual scarps are separated by a break in slope. These may form
 71 in either single or multiple earthquakes. e) A knickpoint forms during a rupture. f) Between rup-
 72 ture events the knickpoint retreats upstream. g) Another knickpoint forms following a subsequent
 73 rupture. The knickpoints are separated by reaches of the river which are at their equilibrium
 74 gradient.



95 **Figure 2.** a) Overview map of Makanjira graben, south Malawi. The Mua and Kasinje seg-
 96 ments are shown by the white box on the Bilila-Mtakataka fault. b) 30 m SRTM DEM and
 97 hillshade for the Mua and Kasinje segments, showing the location of where the major rivers cross
 98 the scarp (identified in the field). c) The number of cells that drain through each cell, i.e. the
 99 discharge capacity, with the inferred drainage basins represented by polygons. Drainage area
 100 (DA) is also given in km².

78 along-strike extent of the fault (Jackson & Blenkinsop, 1997). However, more recent stud-
 79 ies indicate that the fault scarp has a higher degree of along-strike structural complex-
 80 ity and actually consists of at least six geometrically distinct segments (Goda et al., 2018;
 81 Hodge et al., 2018b). UAV data collected on recent field visits also show that the scarp
 82 is more complex than previously described, at least in the few accessible localities.

83 Here we use a very high resolution (< 1 m) point cloud and DEM to detect changes
 84 or breaks in slope on individual scarp profiles and use knickpoint analysis to estimate
 85 the number of ruptures that may have occurred on each segment. In addition, we use
 86 the fault scarp morphology and knickpoint height to estimate the surface offset associ-
 87 ated with each event. We then apply a model of scarp degradation to estimate the dif-
 88 fusion age κt of the scarp profiles, i.e. the amount of erosion that has occurred at the
 89 scarp’s crest since the scarp’s formation. Diffusion age κt , having dimension [length]²,
 90 is the product of diffusivity and chronological age (Andrews & Hanks, 1985). If we as-
 91 sume the diffusivity is constant, this allows us to infer the relative timing of each rup-
 92 ture, and by selecting a typical diffusion constant κ of the region, we can convert diffu-
 93 sion age to chronological age t . Finally, we discuss the processes that formed the cur-
 94 rent BMF scarp and consider future rupture scenarios.

101 **2 Geomorphic indicators of multiple ruptures**

102 **2.1 Complex fault scarps**

103 The morphology of a fault scarp is dependent on many factors, including the type
 104 of earthquake, amount of slip, and the material properties of the surface it displaces. Typ-
 105 ically, a single rupture fault scarp will comprise a free face whose gradient is greater than
 106 the angle of repose of the hillslope sediments (Figure 1a; e.g. Wallace, 1977; Nash, 1984;
 107 Lin et al., 2017). These distinctive free faces, however, erode away within a few hundred
 108 years (e.g. Bucknam & Anderson, 1979; Nash, 1984; Wallace, 1980), forming smoother,
 109 degraded scarp profiles (Figure 1b). When more than a single surface rupture has oc-

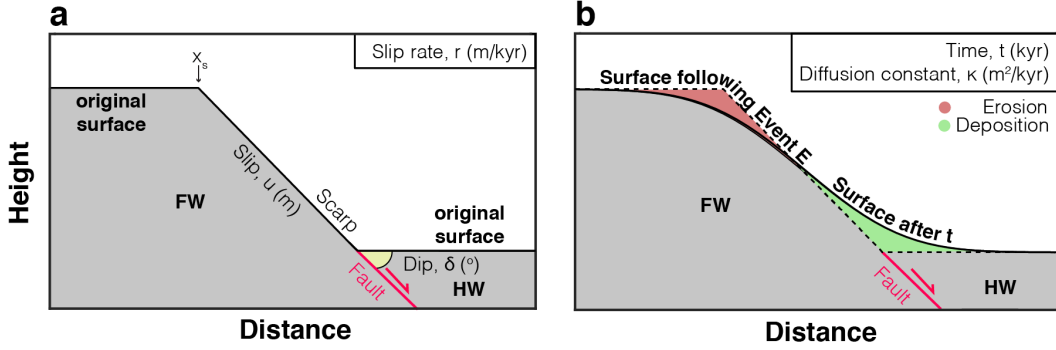
110 curred along a fault, the scarps may comprise either a single scarp face with differing slopes
 111 within it, or an array/stack of multiple discrete scarps set back from one another (Wallace,
 112 1977; Nash, 1984; Crone & Haller, 1991; Zhang et al., 1991; Ganas et al., 2005). Com-
 113 posite scarps comprise a single band of oversteepened terrain where vertical offsets have
 114 accumulated onto the same slope over multiple earthquake cycles (Figure 1c; e.g. Zhang
 115 et al., 1991; Ganas et al., 2005), whereas the vertical offsets of multi-scarps are horizon-
 116 tally offset by terraces (e.g. Nash, 1984; Crone & Haller, 1991). Composite fault scarps
 117 develop when near surface slip is confined to the same fault plane, but multi-scarps form
 118 when slip is confined to a different near-surface fault splay during each earthquake event
 119 (e.g. Slemmons, 1957; Nash, 1984; Anders & Schlische, 1994; Kristensen et al., 2008).
 120 Both multi-scarps and composite scarps can exist along the same fault if a splay is re-
 121 activated as shown in the Serghaya Fault Zone, Syria (Gomberg et al., 2001), the north-
 122 ern Upper Rhine Graben, Germany (Peters & van Balen, 2007) and northern Baja Cal-
 123 ifornia, Mexico (e.g. Mueller & Rockwell, 1995).

124 Multiple surface ruptures on composite scarps may be identified by changes in scarp
 125 slope, marked by slope breaks on the scarp's elevation profile (Figure 1c; e.g. Nash, 1984;
 126 Lin et al., 2017); however, as the scarp degrades, these multiple rupture markers will dis-
 127 appear over time (e.g. Bucknam & Anderson, 1979; Nash, 1984; Wallace, 1980). The ter-
 128 races between individual scarps on a multi-scarp (Figure 1d; e.g. Mayer, 1982) provide
 129 a more lasting record of earthquake activity, but multi-scarps too are considered to de-
 130 grade to a morphology similar to a degraded single rupture fault scarp over sufficient timescales
 131 (e.g. Nash, 1984; Andrews & Hanks, 1985). Understanding whether multiple earthquake
 132 ruptures have occurred on a fault scarp is important as surface displacements may be
 133 used in quantifying paleomagnitude estimates for faults (e.g. Wei et al., 2015; Swan et
 134 al., 1980; Walker et al., 2015), and overestimating slip per earthquake will influence re-
 135 currence interval calculations, and thus the inferred seismic hazard (e.g. Middleton et
 136 al., 2016).

137 2.2 Knickpoints

138 The offset produced by surface ruptures also generates a change in fluvial systems.
 139 Studying the topographical variations within bedrock rivers has been an effective tool
 140 in understanding the evolution of tectonically active landscapes (e.g. Finlayson et al.,
 141 2002; Montgomery & Brandon, 2002). In fluvial geomorphology, the change in the ap-
 142 pearance of a river's longitudinal profile can be a response to tectonic activity (e.g. Ouchi,
 143 1985; Holbrook & Schumm, 1999; Litchfield et al., 2003; Wei et al., 2015; Burbank & An-
 144 derson, 2011). Typically, the longitudinal profile is smooth and concave in appearance;
 145 however, in bedrock channels, surface ruptures can produce knickpoints (Figure 1e; e.g.
 146 Wallace, 1977; Yang et al., 1985; Commins et al., 2005; He & Ma, 2015; Sun et al., 2016).
 147 Over time, knickpoints retreat upstream from their original position during the process
 148 of channel regrading (Figure 1f). As knickpoints migrate upstream they reduce in height,
 149 and may eventually disappear (Holland & Pickup, 1976). Subsequent surface ruptures
 150 can cause additional knickpoints to develop, separated by reaches of the river which are
 151 at their equilibrium gradient (Figure 1g).

152 If the retreat rate is known, the age of formation can be calculated by measuring
 153 the retreat distance, and the knickpoint height may be used (assuming rupture area is
 154 known) to estimate the magnitude of each earthquake event (e.g. He & Ma, 2015; Rosen-
 155 bloom & Anderson, 1994; Sun et al., 2016; Castillo, 2017; Wei et al., 2015). However,
 156 numerical models and field observations have shown that many complex processes in-
 157 cluding sediment flux, channel morphology, channel slope and drainage area contribute
 158 to the rate of knickpoint retreat (Attal et al., 2008; Cowie et al., 2006; Attal et al., 2011;
 159 Whittaker et al., 2007b, 2007a; Gasparini et al., 2006). In the past, analysis of knick-
 160 points was a field-based exercise (e.g. Yang et al., 1985; Rosenbloom & Anderson, 1994);
 161 however, by using high resolution DEMs and mathematical models, knickpoints can be



183 **Figure 3.** Scarp degradation model for soil-mantled fault scarps. a) Parameters used to gener-
 184 ate a catalogue of synthetic fault scarps. FW = Footwall. HW = Hanging-wall. b) Parameters
 185 used for the degradation of a fault scarp profile using a one-dimensional diffusion equation.

162 identified using slope-area relationships and stream gradient calculations (e.g. Howard
 163 & Kerby, 1983; Bishop et al., 2005; Hayakawa & Oguchi, 2006, 2009).

164 3 Numerical model for the formation of multi-scarps

165 Numerical models of fault scarp diffusion have been used to explore the degrada-
 166 tion of composite fault scarps (Avouac & Peltzer, 1993) on the assumption that erosion
 167 is transport-limited as would be the case for soil-mantled landscapes (Arrowsmith et al.,
 168 1998). However, the morphological changes caused by the degradation of multi-scarps
 169 is less well known. Here, we illustrate how the interplay between co-seismic surface off-
 170 sets and degradation causes the formation of multi-scarps using a numerical solution to
 171 the one-dimensional diffusion equation (e.g. Culling, 1963; Nash, 1980; Hanks et al., 1984;
 172 Arrowsmith et al., 1998; Andrews & Hanks, 1985), which calculates changes in elevation
 173 Z along a scarp profile (where x is the horizontal distance) over time t (Figure 3). As-
 174 suming the scarp erosion is transport-limited (where more debris is available for removal
 175 than processes are capable of removing), the vertical component of scarp degradation
 176 is governed by the conservation of mass, and can be applied using the equation (Smith
 177 & Bretherton, 1972):

$$\frac{dZ}{dt} = \kappa \frac{d^2 Z}{dx^2} \quad (1)$$

178 where κ is the diffusion constant (m^2/kyr). Scarp degradation processes transport ma-
 179 terial from the crest of the fault scarp and deposit it at the base of the scarp, smooth-
 180 ing the scarp and reducing the average slope below the fault dip angle δ (Figure 3b). As
 181 the mechanical properties of bedrock are not considered by this equation, it is only strictly
 182 applicable to soil-mantled fault scarps.

186 In our model, an initial scarp is generated at distance x_s along the profile assum-
 187 ing a down-dip, normal sense of displacement on a fault with dip δ , following an earth-
 188 quake of slip u (Figure 3a). We assume an even slip distribution on the fault, including
 189 the surface offset and assume that the slope of the scarp and dip of the fault are equal
 190 following the rupture. By dividing the slip by the fault slip rate r , the time between rup-
 191 tures T_R can be found (also known as the recurrence interval, or return period). Between
 192 earthquakes, the scarp is degraded according to equation 1, and we chose a diffusion con-
 193 stant, κ in the range of 5-10 m^2/kyr suitable for sub-tropical climates. This lies between
 194 values proposed for semi-arid climates (0.5-5 m^2/kyr ; e.g. Hanks et al., 1984; Andrews

195 & Hanks, 1985; Arrowsmith et al., 1996; Carretier et al., 2002; Kokkalas & Koukouvelas,
 196 las, 2005; Nivière & Marquis, 2000) and tropical climates ($10 \text{ m}^2/\text{kyr}$; e.g. Zielke & Strecker,
 197 2009). Estimates for κ may also be affected by vegetation (Hanks et al., 1984). As ex-
 198 pected a larger diffusion constant κ causes more erosion and decreases the slope of the
 199 scarp.

200 The model simulation is run over a fixed period of time T , for a certain number
 201 of events. For multiple ruptures, model parameters (u , r , δ , x_s etc) may be fixed for the
 202 entire simulation period or varied per event. For the fixed parameter scenario, a fault
 203 scarp caused by a single rupture and a composite fault scarp generated by three smaller
 204 ruptures (on the same fault plane) both degraded to identical profiles after a certain dif-
 205 fusion age (Figure 4a,b). For a 60° dipping normal fault the transition from composite
 206 scarps to degraded scarp (i.e. when clear slope break points were removed) occurred at
 207 $\kappa t \sim 36 \text{ m}^2$. For a 40° fault the transition occurred at $\kappa t \sim 20 \text{ m}^2$. For κ in the range
 208 of 5 and $10 \text{ m}^2/\text{kyr}$, this corresponds to a minimum of 2,000 years to create degraded
 209 scarps from composite scarps. Of course, this also depends on many factors that may
 210 have localised influences such as lithology, geological discontinuities (for example, joints),
 211 and moisture content.

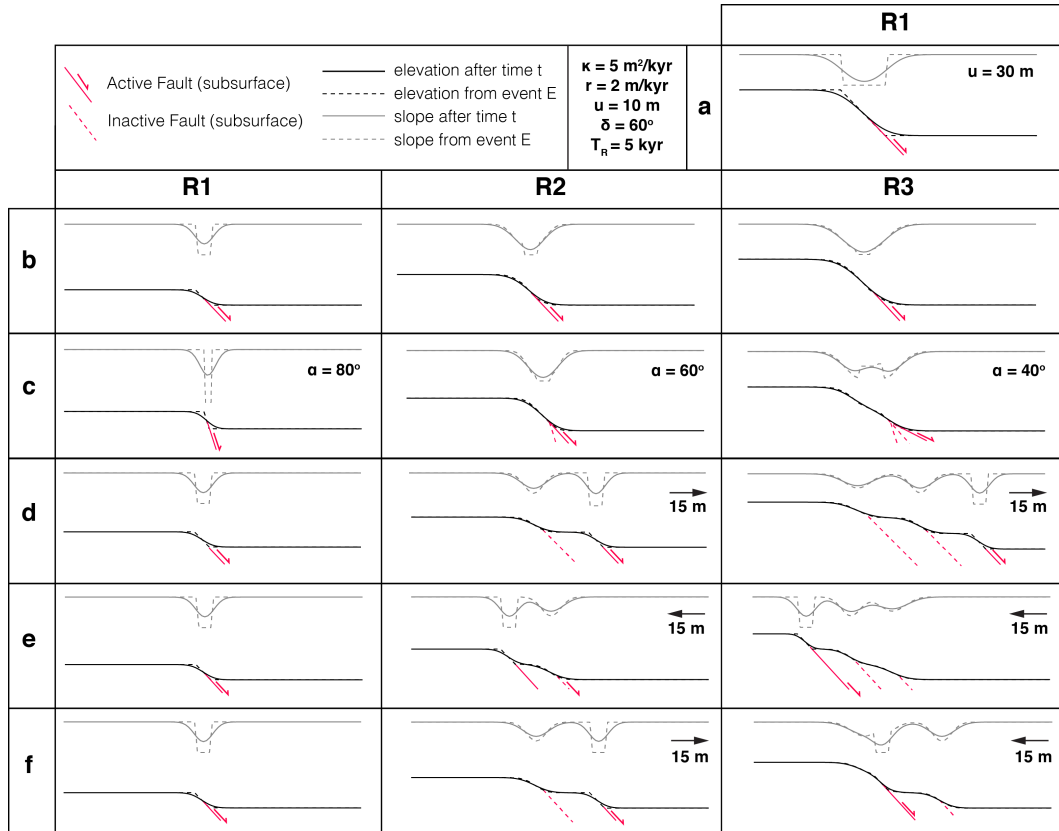
212 Multi-scarps formed during variable parameter simulations which considered de-
 213 creases in fault dip of $> 10^\circ$ per earthquake and changes to the active fault location, i.e
 214 the formation of splays (Figure 4c-f). Moving the active fault plane toward the lower orig-
 215 inal surface created an asymmetric slope profile with a smoother tail toward the scarp
 216 top (Figure 4d), whereas the opposite was observed when the active fault was moved to-
 217 ward the upper original surface (Figure 4e). By alternating the active fault plane between
 218 two parallel surfaces, two composite scarps separated by a break in slope (i.e. a hybrid
 219 composite-multi-scarp) may develop (Figure 4f). The length between the base of one scarp
 220 and the crest of another was slightly smaller than the distance between faults due to the
 221 degradation of two scarp surfaces the terrace separates. These model results illustrate
 222 how degraded multi-scarp and composite scarps have a different morphological expres-
 223 sion (Figure 4). This provides a theoretical framework in which normal fault multi-scarps
 224 can be interpreted, and we now move to an analysis of such scarps in a natural setting.

232 4 Data acquisition and processing

233 4.1 Tectonic setting of the Bilila-Mtakataka fault

234 The Malawi Rift is a 900 km long amagmatic section of the Western Branch of the
 235 East African Rift System (EARS; Ebinger et al., 1987; Ebinger, 1989). It consists of a
 236 series of $\sim 100\text{-}150$ km long grabens and half grabens, which are defined by basin bound-
 237 ing faults (Ebinger et al., 1987; Flannery & Rosendahl, 1990; Laó-Dávila et al., 2015).
 238 The northern and central parts of the Malawi Rift have been flooded by Lake Malawi,
 239 however, its three southernmost grabens are still exposed onshore (Dulanya, 2017; Hodge
 240 et al., 2019). Based on EARS-scale kinematic models, the Malawi Rift is currently ac-
 241 commodating $\sim 2 \text{ mm}/\text{yr}$ east-west extension for a fixed Nubian Plate reference frame
 242 (Saria et al., 2014; Stamps et al., 2018).

243 The BMF lies within the Makankijra Graben and extends for 110 km from the south-
 244 ern end of Lake Malawi to the northern end of the Zomba Graben (Figure 2a). The BMF
 245 is slightly oblique to the current extension direction but is considered to be pure nor-
 246 mal as: (1) no strike-slip offsets have been observed in the field or in DEMs (Hodge et
 247 al., 2018a), and (2) it is broadly parallel to the structure that may have been the source
 248 of the 1989 Salima earthquake, which had a rake of $-92^\circ \pm 25^\circ$ and an epicentre 40 km
 249 north of the BMF's surface expression (Jackson & Blenkinsop, 1993). This apparent di-
 250 chotomy between its normal kinematics and slight obliquity to the regional extension di-
 251 rection can be explained by the presence of a deep-seated crustal weakness (Philippon



225 **Figure 4.** The synthetic fault scarp formation and degradation. a) A single rupture scarp. b)
 226 A composite scarp formed by three equally-sized ruptures (R1, R2 and R3). Panels c-f) Multi-
 227 scarps formed by: c) decreases in fault dip δ per rupture; d) movement of the active fault plane
 228 (solid red line) into the hanging-wall; e) movement of the active fault plane into the footwall; and
 229 f) alternating the active fault between two fault planes. The dashed lines denote the elevation
 230 (black) and slope (grey) profiles immediately following the rupture. The solid lines denote the
 231 profiles at the end of the recurrence interval T_R .

252 et al., 2015; Hodge et al., 2018b), consistent with structural analysis that shows normal
 253 faults with a range of orientations can be reactivated within a uniform stress field (Williams
 254 et al., 2019).

264 The BMF juxtaposes amphibolite-grade Proterozoic gneisses and granulites in the
 265 footwall against post-Miocene sediments in the hanging wall (Walshaw, 1965; Jackson
 266 & Blenkinsop, 1997; Dulanya, 2017; Hodge et al., 2018b). The landscape is soil mantled,
 267 albeit with some rocky outcrops (Figure 5a-b). In contrast, river channels are rocky with
 268 little sediment remaining in the channels (Figure 5c-d). This is consistent with the stan-
 269 dard assumptions for the geomorphological analyses performed here, namely that 1) degra-
 270 dation of the scarp is transport-limited and 2) retreat of the knickpoints is detachment-
 271 limited (Whipple & Tucker, 1999; Arrowsmith et al., 1998).

276 4.2 Data processing

277 To determine whether the Bilila-Mtakataka fault scarp records multiple earthquake
 278 events, as is qualitatively observed (Figure 6), we use a sub-metre point cloud generated
 279 from Pleiades imagery (Hodge et al., 2019). Because of the size of the point cloud (in
 280 excess of 30 GB), to save computational resources we restrict our study area to the two
 281 major segments at the centre of the BMF: the Mua and Kasinje segments (Figure 2b,
 282 S1) that are found to contain the largest scarps (> 20 m high) along the entire fault (Hodge
 283 et al., 2018b, 2019). Both the average height of these segments and the average scarp
 284 height (used as a proxy for vertical displacement; e.g. Morewood & Roberts, 2001) along
 285 the entire fault (~ 14 m) exceed the magnitude of slip typical of a single event for a fault
 286 the length of the BMF (< 10 m; Scholz, 2002). Therefore, due to this and their central
 287 location along the BMF, the Mua and Kasinje segments may be the most likely segments
 288 to show evidence of multiple ruptures at the surface.

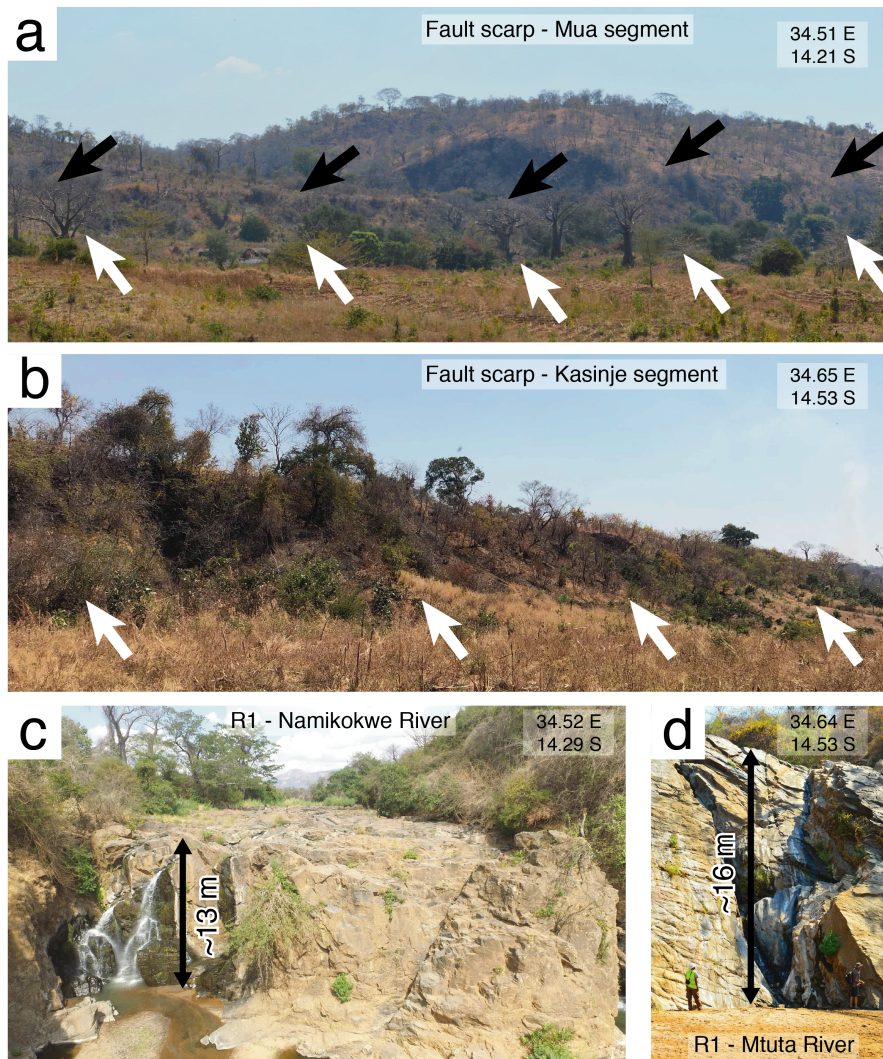
289 The BMF scarp is soil-mantled and the area surrounding it is densely vegetated
 290 (Figures 2b, 5a-b, 6 and S1), which causes significant, local fluctuations in elevation data
 291 (Hodge et al., 2019). When this noise propagates into slope calculations, it affects scarp
 292 parameter calculations, and so to analyse the sub-metre point cloud used in this study,
 293 we first improve the signal-to-noise ratio. To mask vegetation, a normalised difference
 294 vegetation index (NDVI) is calculated from the red (R) and near-infrared (NIR) bands
 295 (e.g. Elvidge & Lyon, 1985; Grigillo et al., 2012; Rawat & Joshi, 2012; Yu et al., 2011):

$$NDVI = \frac{NIR - R}{NIR + R} \quad (2)$$

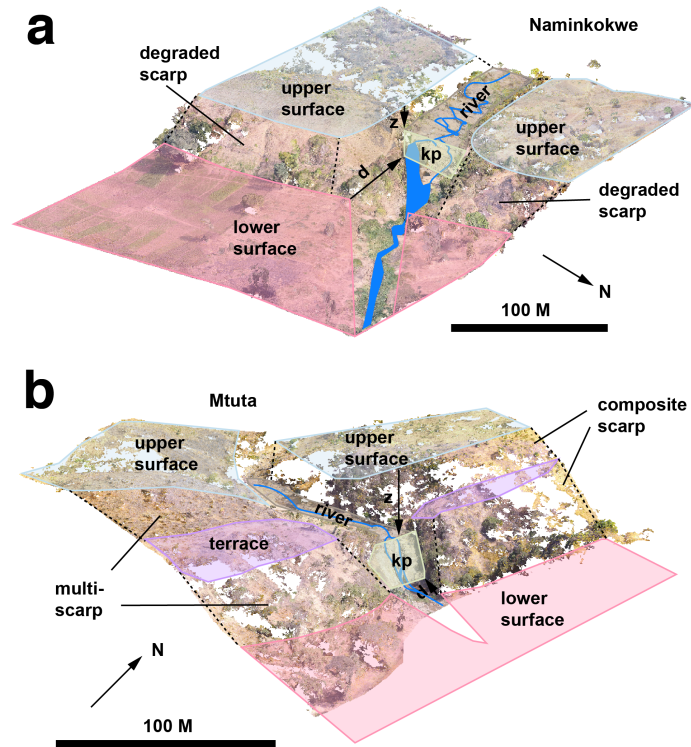
296 For 50 representative sample points, the median NDVI value for vegetated and non
 297 vegetated areas was found to be 0.57 and 0.33, respectively (Figure S1). Non vegetated
 298 areas were also found to have a larger composite RGB value than vegetated areas (i.e.,
 299 they are lighter in RGB colour). The best performing NDVI threshold to reflect the tran-
 300 sition to vegetation was 0.45, where just 4% of sample points were incorrectly identified
 301 ($n=100$, Figure S1). Note, this is higher than previous studies which have reported that
 302 a NDVI value greater than 0.2 coincides with vegetation coverage (Grigillo et al., 2012).
 303 However, this difference may be due to differences in camera calibration and colour lev-
 304 els. In addition, we manually remove additional large-scale noise features such as build-
 305 ings that cannot be captured using the NDVI method.

306 4.3 Scarp profiles

307 Twenty-one scarp profiles along the Mua segment and eighteen from the Kasinje
 308 segment were identified as having a sufficient point cloud density ($> 90\%$ coverage and
 309 no gaps > 10 m) to be analysed (Figure S1). To account for geometrical variations along
 310 the segments influencing our vertical displacement calculations (e.g. Mackenzie & El-



255 **Figure 5.** Field photos of the Bilila-Mtakataka fault scarp (a-b) and knickpoints (c-d). a)
 256 Fault scarp along the Mua segment. b) Fault scarp along the Kasinge segment. White arrows
 257 indicate the base of the scarp, black arrows the top of the scarp. The scarps are soil mantled,
 258 with occasional rocky outcrops, consistent with the behaviour of hillslopes (and thus fault scarps)
 259 that erode in a diffusive manner. c) Knickpoint R1 along the Namikokwe River. d) Knickpoint
 260 R1 along the Mtuta River. The height of each knickpoint was estimated using photo analysis and
 261 corresponds well with the R1 knickpoint heights extracted from the Pleiades imagery (Figures 11
 262 and 12). The rocky river channels shown here suggests that the retreat of these knickpoints is a
 263 detachment limited process.



272 **Figure 6.** Oblique views of the Bilila-Mtakataka fault scarp from a drone-based Digital Ele-
 273 vation Model. a) Naminkokwe River (Mua segment), b) Mtuta River (Kasinje segment). These
 274 images show local evidence for composite and multi-scarps. Knickpoints (kp) are clearly visible in
 275 both rivers.

311 liott, 2017), profiles were oriented to perpendicular to the average trend of the BMF (150°)
 312 (Hodge et al., 2018b). For each profile, points were taken at intervals of a half-metre.
 313 The minimum scarp profile length is 300 m.

314 Despite improving the signal-to-noise ratio, we find that local noise still results in
 315 variations in the gradient with an amplitude comparable to that expected by a scarp or
 316 knickpoint. To further improve the signal-to-noise ratio, we apply a digital filter to the
 317 elevation profiles. We use the *rloess* function in MATLAB as a filter, which is a more
 318 robust version of the Loess filter (Cleveland, 1981). The quadratic regression used by
 319 *rloess* is more computationally expensive than the Loess filter, but is better at remov-
 320 ing outliers whilst not without drastically influencing the elevation or slope profiles (Hodge
 321 et al., 2019). As we do not want to artificially reduce the scarp slope or smooth over slope
 322 breaks, we choose a bin width of 15 m. Smaller window sizes failed to successfully elim-
 323 inate background noise close to scarps.

324 4.4 River profiles

325 The rocky character of the rivers and streams in this area (Figure 5c-d) suggests
 326 knickpoint positions and retreat rates may encode information about the downstream
 327 faults tectonic history. The geological map by Dawson and Kirkpatrick (1968) shows the
 328 Naminkokwe River as the only major river that crosses the BMF scarp, but during field-
 329 work we identified two additional rivers that are suitable for knickpoint analysis; the Livezezi
 330 and Mtuta rivers (white circles Figure 2b). The Naminkokwe River is located at the north-
 331 ern end of the Mua segment (~ 37 km from the northern end of the fault). It is ~ 10
 332 m wide on average, including where it crossed the fault scarp, but has a prominent 20
 333 to 30 m wide section between 50 and 200 m from the scarp. The Livezezi River, which
 334 is located at the intersection between the Mua and Kasinje segments (near the town of
 335 Golomoti), is reasonably well-defined where it crosses onto the valley floor, comprising
 336 a width of around 20 m. Upstream the river is locally up to 100 m wide, but averages
 337 ~ 30 m. The larger channel width of the Livezezi River compared to the Naminkokwe
 338 River suggests it has a larger flow discharge (Leopold & Maddock, 1953). The Mtuta River,
 339 has a maximum width of ~ 10 m, but had significantly less discharge passing through
 340 it than the other rivers observed during fieldwork in the dry season. We identified 4 smaller
 341 unnamed channels using the DEM, and since these are < 5 m wide, we refer to them as
 342 streams, and label them according to their location within the segment: Mua north, Mua
 343 South, Kasinje North and Kasinje South (grey circles, Figure 2b). During the fieldwork,
 344 no discharge passed through each stream. How discharge changes during the wet sea-
 345 son for each river and stream is unknown to us currently.

346 Each channel was traced from the Pleiades point cloud using the polyline tool in
 347 CloudCompare[®]. The nearest point from the Pleiades point cloud to the polyline was
 348 selected within a parallel distance of 2 m, at an interval of a half-metre. The extracted
 349 point cloud was manually cleaned to remove noise. Because of smaller channel widths,
 350 the streams had more noise due to overhanging vegetation from the channel sides. This
 351 resulted in significant gaps in the extracted profiles for some streams. The points were
 352 then plotted along the length of the detailed channel, to form a two-dimensional profile
 353 where the horizontal axis is the distance from the fault scarp. As a smoothed longitudi-
 354 nal profile also better represents the true channel bottom (Wei et al., 2015), we apply
 355 a digital filter to improve the signal-to-noise ratio. As we want to preserve the vertical
 356 to sub-vertical gradients of the knickpoints to identify them in the river profiles, we use
 357 a Savitzky-Golay filter, which is based on local least-squares polynomial approximation
 358 (Savitzky & Golay, 1964) and helps preserve data features such as peak height and width.
 359 Due to the large elevation artefacts of the noise on the channels, we set the window size
 360 to be 20 m. Although all the channels show a clear downslope trend, there are sections
 361 that show a small, localised upslope trend, which is likely the result of vertical or hor-
 362 izontal uncertainty. The vertical uncertainty may be a few meters, especially where parts

of the scarp are far away from ground control points (GCPs) used to develop the DEM from the stereo-pair. Similarly, our polyline may not follow the true channel, for example, if there is a lower section adjacent to the selected point or there is overhanging vegetation cover that was not removed by the filter. However, these minor upslope trends could also be real, and may be overcome by the increased channel flow velocity and height during the wet season.

River drainage area is considered to be an important factor in the speed at which a knickpoint retreats through a river system (e.g. Berlin & Anderson, 2007; Seidl et al., 1994; Hayakawa & Oguchi, 2006; Bishop et al., 2005; Crosby & Whipple, 2006). We performed a hydrological analysis on a 30 m SRTM DEM in QGIS (Figure 2b) to compute drainage direction and discharge capacity (Figure 2c). A polygon was then drawn around the tributaries that drained into each river or stream at the point they incised the scarp to reflect the estimated drainage area (Figure 2c). As we are not certain of the hydrological processes acting over the Chirobwe-Ncheu fault to the west, and whether discharge flows over this fault and into the rivers or streams in this study, our polygons do not extend into the footwall of this fault. The results show that the Livelezi River has a drainage area in excess of 200 km², the Naminkokwe and Mtuta Rivers have drainage areas of 43 km² and 32 km² respectively, and the four smaller streams have drainage areas < 20 km².

5 Fault scarps

5.1 Scarp analysis methods

Using the characteristics typical of single or multiple surface ruptures on fault scarps (Figure 1), we categorise each profile as either: (i) a single rupture scarp, (ii) a degraded scarp, (iii) a composite scarp, or (iv) a multi-scarp. Scarp surfaces are marked by steep gradients and troughs in the calculated slope profile. Slope breaks are marked by gentle gradients separating multiple troughs. For composite scarps, the number of ruptures is quantified by the number of slope changes (i.e. pairs of major slope break points), and for multi-scarps, the number of slope breaks. We note that degraded scarps may be fault scarps that have experienced multiple ruptures, but have undergone sufficient degradation for individual rupture markers to be lost (e.g. Bucknam & Anderson, 1979; Nash, 1984; Wallace, 1980). As a result, for all scarp types the number of ruptures is a minimum estimate.

The total scarp height H for each profile was calculated as the cumulative surface displacement along the fault (Figure 7a,b; Hodge et al., 2018b). First, the crest and base of the entire scarp (regardless of whether it contains multiple rupture indicators) were picked manually, then a regression line was fitted to the upper and lower original slopes. The scarp height is then calculated as the difference between the two regression lines at a location corresponding to the maximum slope on the scarp surface.

For multi-scarp profiles, the crest and base of each individual scarp surface (identified by breaks in slope) were manually picked and the scarp height of each calculated using the regression line method (Figure 7b). As scarps smooth over time due to degradation (e.g. Bucknam & Anderson, 1979; Nash, 1984; Wallace, 1980), and as the lithology along both segments is uniform at fault-scale (Walshaw, 1965; Hodge et al., 2018b) implying limited spatial variability in diffusivity, we order the scarp surfaces in terms of slope steepness: from steepest to gentlest. We then infer the steepest surface to be a less degraded, younger scarp surface and hence represent the most recent rupture event (R1), the next steepest surface to represent the next most recent rupture event (R2), and so forth. We note that the most recent surface rupture here denotes the most recent 'observable' surface rupture, where a more recent surface rupture may have occurred but may have been too small to identify, or eroded away. The horizontal distance between

412 scarp surfaces (i.e. between one scarp surfaces base and another's crest) was also mea-
 413 sured for multi-scarps.

414 For composite scarps, the scarp height of R1 (H_{R1}) - identified as the steepest scarp
 415 surface at the centre of the scarp - was calculated by fitting a regression line to the R2
 416 surfaces and calculating the elevation difference at the location corresponding to the max-
 417 imum slope on the R1 scarp surface (Figure 7a). The scarp height of earlier rupture events
 418 are then found by calculating the elevation difference (Z) using the regression line ap-
 419 proach and the next older rupture surface, or original surfaces if calculating the oldest
 420 rupture, and subtracting the cumulative scarp heights of subsequent ruptures, i.e. $H_{Rn} =$
 421 $Z - \sum_{i=1}^{n-1} H_{Ri}$.

438 5.2 Results of scarp analysis

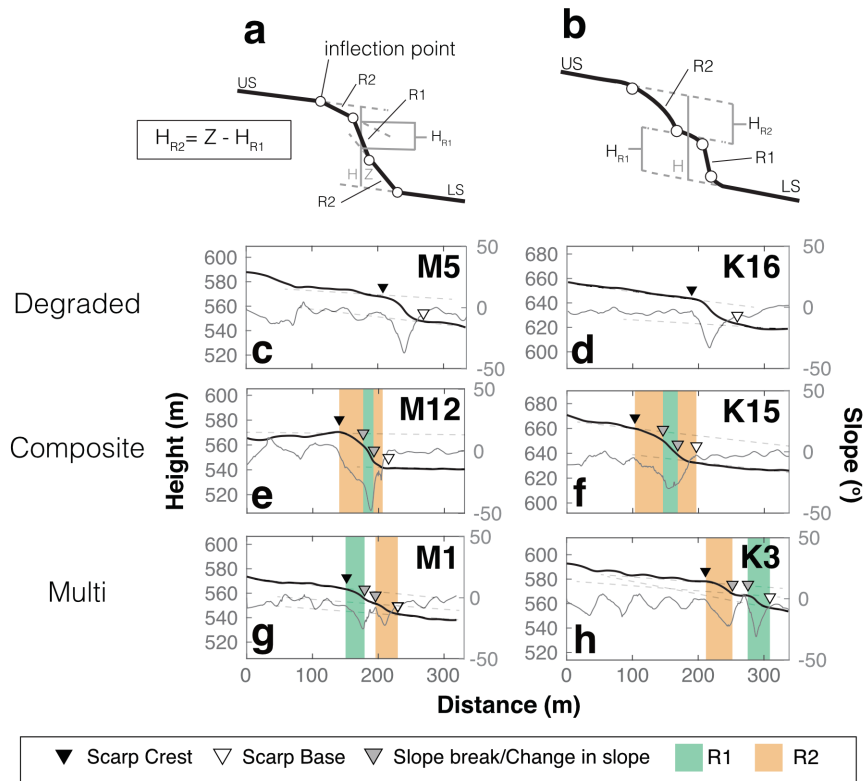
439 The average total scarp height for all profiles was 22 ± 5 m; the average total scarp
 440 height for Mua profiles was slightly smaller (21 m) than Kasinje (22 m), but had a smaller
 441 standard deviation (6 m compared to 7 m, Figure 8c). On average, the total scarp height
 442 is larger at the centre of the segments than the edges, as has been previously observed
 443 (Hodge et al., 2018b, 2019). For several kilometres toward the intersegment zone (Livezezi
 444 River), the total scarp height for both segments decreases by up to 15 m; however, the
 445 local scarp height near the river increases by up to 10 m on both segments.

446 Figure 7c-h shows examples of degraded, composite and multi- scarps from the Mua
 447 and Kasinje segments. As no free faces were identified on any profile, none were cate-
 448 gorised as a single rupture scarp (i.e., fresh scarp that formed in the last few decades).
 449 Profiles M5 and K16 are examples of degraded fault scarps, displaying a smooth eleva-
 450 tion profile and symmetrical slope profile. M12 and K15 however show an increase in slope
 451 toward the scarp centre (highlighted green in Fig. 7e,f), typical of a recent rupture on
 452 a pre-existing scarp; these profiles are interpreted as composite scarps. Breaks in slope
 453 typical of multi-scarps can be found on M1 and K3, where the steepest scarp surface is
 454 shown in green in Fig. 7g,h.

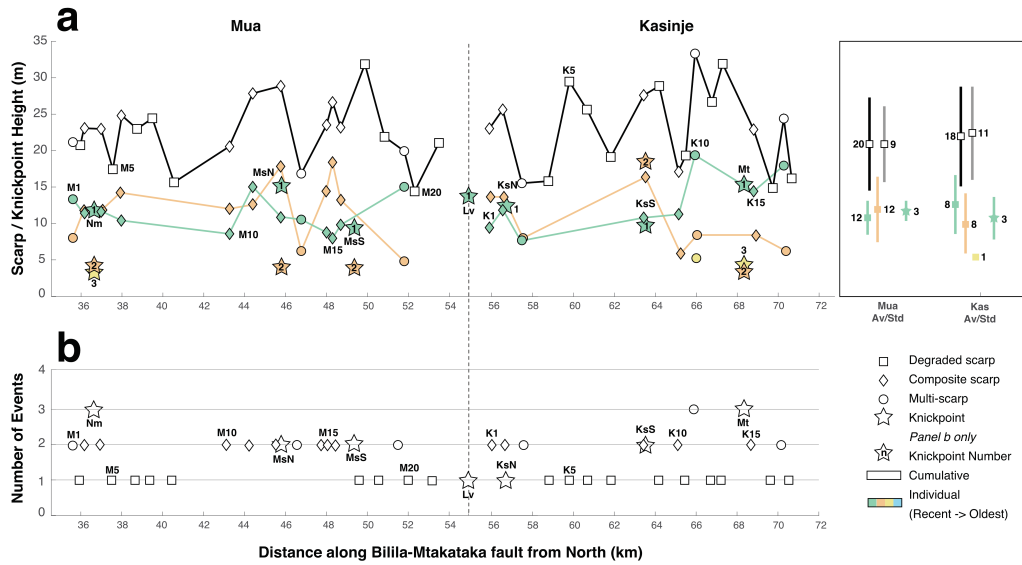
455 Out of the 39 profiles, 19 were categorised as degraded scarps (nine on Mua, 10 on
 456 Kasinje), 14 as composite scarps (nine on Mua, five on Kasinje), and six as multi-scarps
 457 (three on both Mua and Kasinje). For multi-scarps, the steepest scarp surface (R1) was
 458 nearest the lower original surface for all but one profile (M1). For the 20 profiles where
 459 multiple events could be identified (i.e. composite scarps or multi-scarps), all but one
 460 showed evidence for two subscarps (R1 and R2, Figure 8b). The anomalous result, multi-
 461 scarp profile K12, has an additional break in slope (R3).

462 Our numerical model demonstrated that multi-scarps are formed by fault splays
 463 (Figure 4d-f), which is consistent with rupture of anisotropic rocks leading to the acti-
 464 vation of different surfaces (e.g. Lee et al., 2002; Hodge et al., 2018b). Here, the major-
 465 ity of the multi-scarps on the two BMF segments were recorded at segment tips. This
 466 is consistent with fault splay formation at segment tips observed in other natural exam-
 467 ples (Manighetti et al., 2001; Wu & Bruhn, 1994; Giba et al., 2012; Segall & Pollard, 1983),
 468 as well as experiments and theoretical models (Perrin et al., 2016a, 2016b; Willemse &
 469 Pollard, 1998).

470 For the degraded scarps, the average scarp heights were 21 ± 5 m and 22 ± 5 m, re-
 471 spectively for Mua and Kasinje. The total scarp heights for composite scarps and multi-
 472 scarps was ~ 23 m for both segments and therefore comparable to the average height
 473 of the degraded scarps. For composite scarps and multi-scarps, the scarp height of R1
 474 was on average 11 ± 2 m for the Mua segment, and 13 ± 4 m for the Kasinje segment (green
 475 symbols, Figure 8a). For the Mua segment, the R1 scarp height was fairly constant, whereas
 476 it was more variable on the Kasinje segment and increased southward. The scarp related
 477 to R2 (orange symbols, Figure 8a) had a height of 12 ± 4 m and 10 ± 4 m for Mua and Kas-



422 **Figure 7.** Schematic showing a) composite scarp and b) multi-scarp profile. a) The scarp
 423 height of the most recent rupture event R1 (H_{R1}) is calculated by fitting a regression line to the
 424 R2 rupture surfaces and calculating the elevation difference at the location corresponding to the
 425 maximum slope on the R1 scarp surface. The scarp height of a subsequent rupture event (i.e.
 426 H_{R2}) is then found by calculating the elevation difference (Z) using the regression line approach
 427 and the next older rupture surface, or original surfaces if calculating the oldest rupture, and
 428 subtracting the cumulative scarp heights of earlier ruptures (i.e. H_{R1}). b) Regression lines are
 429 fitted to the upper (US) and lower (LS) original surfaces, and the terraced surface (slope break)
 430 between scarps. The scarp height for each rupture event is then calculated as the elevation dif-
 431 ference between regression lines at the slope maxima. c-h) Three examples from the Mua (c,e,g)
 432 and Kasinje segments (d,f,h): a degraded scarp with no indicators of multiple ruptures (c,d), a
 433 composite scarp with multiple events (e,f), and a multi-scarp with multiple rupture events (g,h).
 434 Filled black triangles denote the crest of the entire fault scarp. Filled white triangles denote the
 435 scarp base. Filled grey triangles denote breaks or changes in slope between individual scarp sur-
 436 faces formed by multiple ruptures. The steepest surfaces corresponding to R1 are coloured green,
 437 and the gentler surfaces corresponding to R2 are coloured orange.



480 **Figure 8.** a) The total scarp height for scarp profiles (white filled), against individual scarp
 481 heights for the last rupture event (R1; green), penultimate rupture event (R2; orange), and third
 482 rupture event (R3; yellow), for scarp analyses. The box at the end of the profile shows the aver-
 483 erage (squares) and standard deviation (error bars) values for the scarp height of the following:
 484 total (black), degraded (grey), R1 (green), R2 (orange), and R3 (yellow). Knickpoint results are
 485 shown as stars corresponding to the inferred rupture event. b) The number of rupture events
 486 inferred from the scarp profiles (square = degraded scarps, diamond = composite scarps, circle =
 487 multi-scarps) and knickpoints (stars) for the Mua and Kasinje segments.

478 inje, respectively. The scarp height of R2 is greatest at the centre of the segments. A third
 479 subsarp (R3) on profile K12 was identified, comprising a scarp 5 m high.

488 5.3 Estimating diffusion age

489 Previous studies have applied the scarp degradation model shown in Figure 3 to
 490 natural fault scarps in soil-mantled landscapes. Using the slip and slip rate along a fault
 491 to estimate the date of the scarp-forming earthquake or earthquakes, it is possible to cal-
 492 culate the diffusion constant κ (e.g. Avouac & Peltzer, 1993; Arrowsmith et al., 1998;
 493 Carretier et al., 2002). For the Bilila-Mtakataka fault, neither the date of past earthquakes
 494 nor the slip rate is known so we cannot directly estimate the diffusion constant κ . In-
 495 stead we estimate the diffusion age κt (i.e. the amount of erosion that has occurred on
 496 the scarp since the earliest earthquake). Note, the term diffusion age is widely used in
 497 the literature but is misleading as it actually corresponds to the area given by the prod-
 498 uct of diffusivity κ and chronological age t (Andrews & Hanks, 1985). By making some
 499 assumptions about κ , we may then be able to convert κt to find the relative differences
 500 in age between scarp profiles.

501 We estimate the age of the 33 composite or degraded scarp profiles along the Mua
 502 and Kasinje segments shown in Figure 8a. As the negative change in elevation at the up-
 503 per portion of the scarp should correspond to an equal positive change in elevation at
 504 the bottom of the scarp, only the erosion at the upper scarp needs to be calculated. First,
 505 the intersection is found between a regression line fitted to the upper surface and one

506 fitted to the scarp surface. The two regression lines are then joined to reproduce the orig-
 507 inal scarp surface before degradation. Using equation 1 the initial scarp is degraded over
 508 a period of time of T at intervals of t . We assume a fault dip of 60° in the absence of
 509 other information. At each step, the goodness of fit is assessed by comparing the mod-
 510 elled scarp profile against the observed scarp profile by estimating the root mean square
 511 error (RMSE). Confidence intervals are defined by considering profiles within a 5 cm range
 512 of RMSE_{min} (Avouac & Peltzer, 1993; Arrowsmith et al., 1998).

513 The average diffusion age for the 33 scarp profiles is $48 \pm 25 \text{ m}^2$ with a range of \sim
 514 1 to 98 m^2 . Minimum misfit (RMSE_{min}) between forward model and observations varies
 515 from less than 0.1 m (e.g., profiles M3, M17, K5 and K13) to ~ 1 m (profile M9), with
 516 an average of ~ 0.2 m. Profile M2 is an example of a reasonably well fitting profile (RMSE_{min}
 517 0.3 m) for a small diffusion age ($11 \pm 8 \text{ m}^2$; Figure 9a). In comparison, profile K2 was es-
 518 timated to have a similarly low diffusion age ($16 \pm 5 \text{ m}^2$), but the model fit was worse (RMSE_{min}
 519 0.4 m, Figure 9b). The poor fit for profile K2 is due to the variable scarp slope near the
 520 scarp crest, a feature typical of composite scarps. In comparison profile M2 is a degraded
 521 scarp and therefore has a smoother slope profile. Profile M8 is an example of a scarp that
 522 has a large estimated diffusion age ($98 \pm 17 \text{ m}^2$), where the fit between the model and ob-
 523 servations were good but uncertainty was large (RMSE_{min} 0.1 m, Figure 9c). The in-
 524 verse solution of the model estimated a κt of just $\sim 1 \text{ m}^2$ for profile M9, but the RMSE_{min}
 525 was ~ 1 m, indicating a very poor fit.

526 In general, a better model fit was found for scarps with a larger diffusion age (Fig-
 527 ure 10b). Of the 18 profiles whose κt is estimated to be less than 50 m^2 , six have a RMSE_{min}
 528 of 0.3 m or greater (M4, M9, M10, M11, K1 and K2), whereas only one profile has an
 529 equivalent RMSE_{min} where κt is $> 50 \text{ m}^2$ (M6). Smaller scarps typically have a smaller
 530 κt than larger scarps (Figure 10c). The smallest scarp (K16, ~ 15 m high) has a κt of
 531 $\sim 24 \pm 7 \text{ m}^2$, whereas the largest scarp (M17, ~ 31 m high) has a κt of $\sim 65 \pm 8 \text{ m}^2$. Pro-
 532 file M20 is the anomalous result to this relationship, where a ~ 14 m high scarp has a
 533 κt of $80 \pm 17 \text{ m}^2$. This scarp is located within 5 km of the intersegment zone. Typically,
 534 Mua segment scarps close to the intersegment zone have larger estimated κt values than
 535 those at comparable distances on the Kasinje segment (Figure 10a).

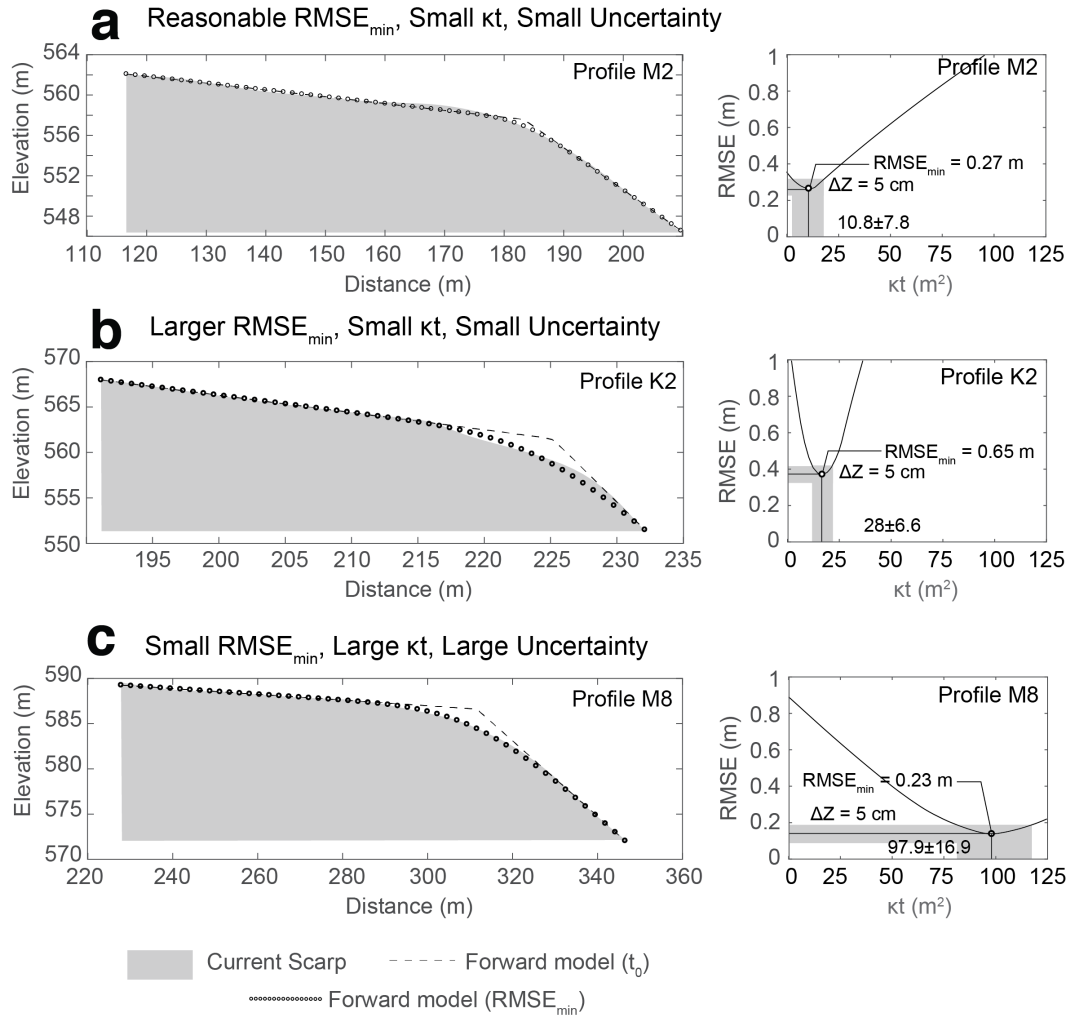
536 The Mua and Kasinje segments have the same average κt value within error (Fig-
 537 ure 10a). The estimated κt value for the Mua segment is $52 \pm 24 \text{ m}^2$ ($n=18$) and for the
 538 Kasinje segment is $42 \pm 26 \text{ m}^2$ ($n=15$). For both segments, degraded and composite scarps
 539 have a similar average diffusion age ($\sim 50 \text{ m}^2$), but degraded scarps have a larger stan-
 540 dard deviation. This may imply that there is no major difference in diffusion (or age)
 541 between the two types of scarps. Profiles M8 and K6 have the largest estimated diffu-
 542 sion age ($95 \pm 20 \text{ m}^2$) and M2 and K4, the smallest ($11 \pm 0 \text{ m}^2$, Figure 10a). This is likely
 543 due to the steep surface near the scarp crest, which the model could not fit a reasonable
 544 degraded surface to. Typically, κt values are lower at the segment ends than the centre,
 545 but variations do occur (Figure 10a).

553 6 Knickpoints

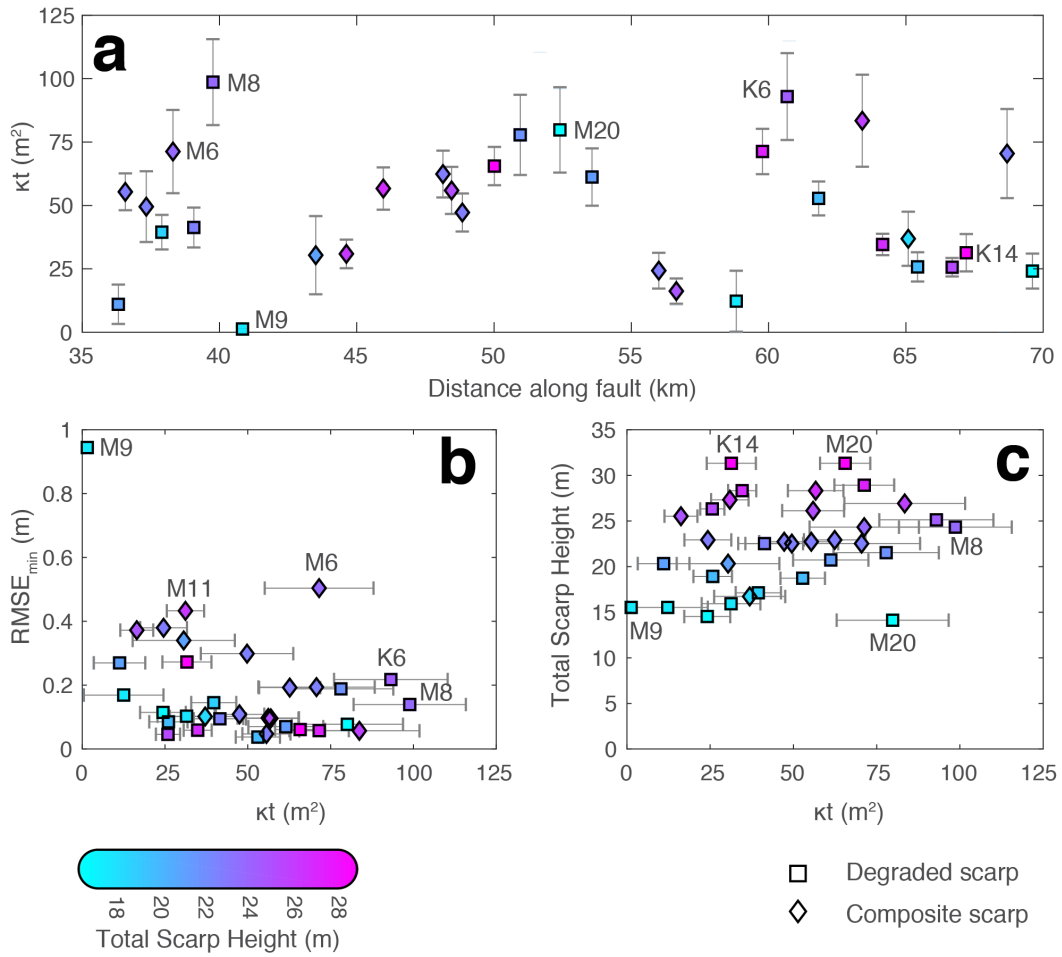
554 We calculate the gradient of each river profile using a rolling window of length d :

$$G_d = \frac{e_2 - e_1}{d} \quad (3)$$

555 where e_1 and e_2 are elevations at $d/2$ either side of the measurement point respectively.
 556 The value of G_d changes as a function of d in response to the local riverbed morphol-
 557 ogy (Wei et al., 2015). Here, we test a d of 10 and 70 m and find that the best value for
 558 our data is $d = 10$ m, but large knickpoints could still be identified using $d = 70$ m
 559 (Figure 11). Attempts have been made to automate knickpoint identification using G_d



546 **Figure 9.** Diffusion age (κt) calculations for three selected examples: a) Profile M2 where
 547 a reasonable $RMSE_{min}$ (0.27) was found for a κt of $11 \pm 8 \text{ m}^2$, b) profile K2 where a large
 548 $RMSE_{min}$ (0.65) was found for a κt of $28 \pm 7 \text{ m}^2$, and c) profile M8 whose $RMSE_{min}$ of 0.23
 549 shows a good model fit to a κt of $98 \pm 17 \text{ m}^2$.



550 **Figure 10.** Diffusion ages κt for scarp profiles across the Mua and Kasinje segments of the
 551 Bilila-Mtakataka fault. a) the estimated κt plotted against the distance along the fault; b)
 552 $RMSE_{min}$ versus κt , and c) total scarp height versus κt .

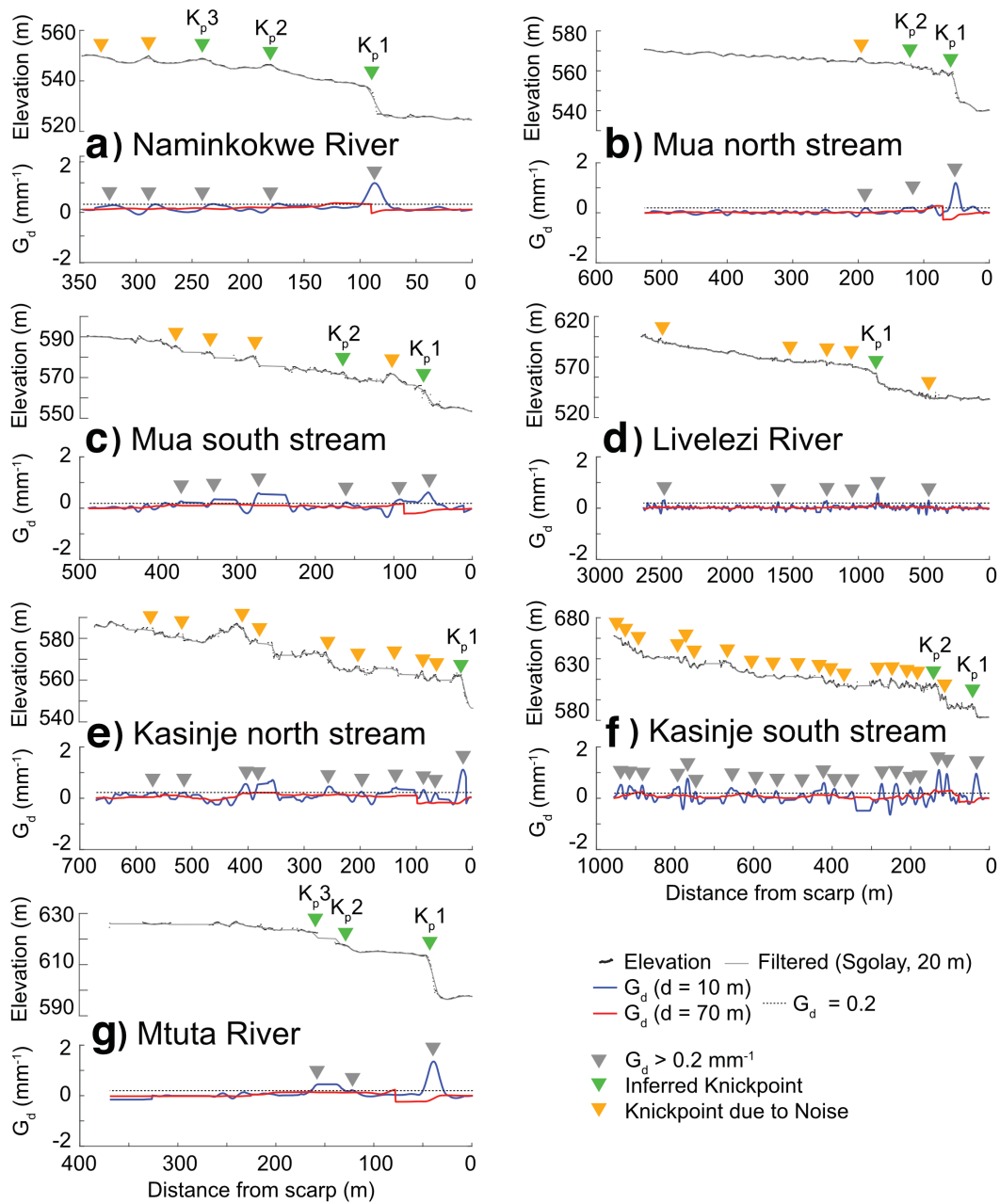
560 (Hayakawa & Oguchi, 2006); however, choosing an appropriate threshold value to ob-
 561 jectively define knickpoints is challenging for small drainage areas (Wei et al., 2015). Here,
 562 we choose $G_d > 0.2$ and manually analyse smaller peaks.

563 To identify which knickpoints are caused by faulting, we follow the criteria proposed
 564 by Wei et al. (2015): 1) knickpoints are only considered if they are located upstream of
 565 the fault scarp (i.e. in the footwall); 2) we exclude candidates if the elevation fluctuates
 566 considerably on either side of the point; and 3) we use geological and topographical maps,
 567 to exclude points positioned at lithologic contacts, at the confluence of tributaries and/or
 568 bends in the river profile (Wohl, 1993). We note that regional geological maps may not
 569 account for local lithological variation, a possible source of error within the profiles. We
 570 number the knickpoints for each stream chronologically based on their distance from the
 571 scarp (i.e. $K_p1, K_p2 \dots K_pn$).

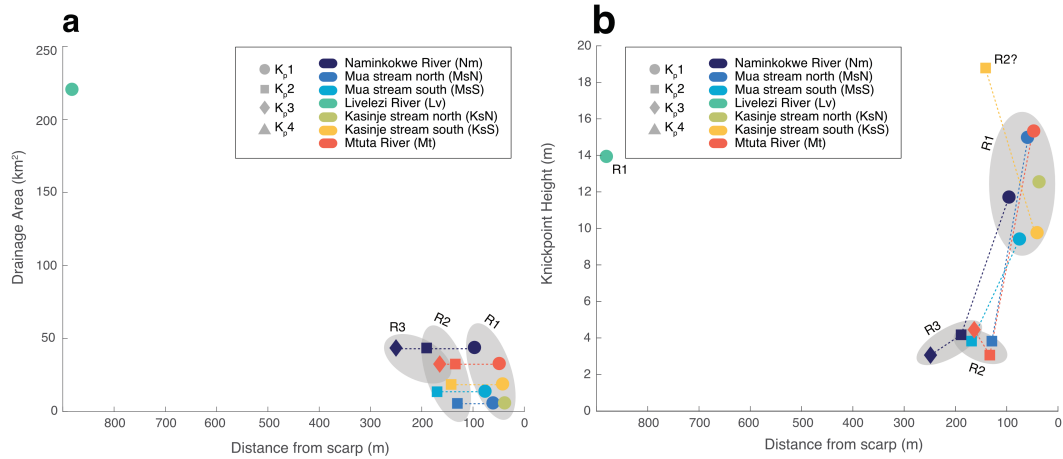
580 Each river or stream has at least one inferred knickpoint, K_p1 (Figure 11). The first
 581 knickpoint is well defined, and is usually located within 100 m of the fault scarp. The
 582 larger distance of K_p1 on the Livelezi River (~ 900 m) may suggest that the retreat rate
 583 on the Livelezi is faster than the others, consistent with its larger discharge rate (assumed
 584 by its larger width) and drainage area (Figure 12a; e.g. Berlin & Anderson, 2007; Seidl
 585 et al., 1994; Hayakawa & Oguchi, 2006; Bishop et al., 2005; Crosby & Whipple, 2006).
 586 The river with the second largest drainage area/discharge is the Naminkokwe River (Dawson
 587 & Kirkpatrick, 1968), whose K_p1 is setback the second furthest from the scarp (~ 95 m).
 588 A second knickpoint K_p2 was identified on five of the profiles (Naminkokwe and Mtuta
 589 rivers, both Mua streams and the northern Kasinje stream), but not on Livelezi River.
 590 Where identified, K_p2 is setback between 130 and 190 m from the scarp (Figure 11). A
 591 third knickpoint K_p3 was identified on both the Naminkokwe and Mtuta rivers and is
 592 setback 160 to 250 m from the scarp. The lack of additional knickpoints on the Livelezi
 593 River may be due to the larger catchment area and discharge rate causing knickpoints
 594 to migrate upstream at a faster rate, beyond the limits of our profile (Wallace, 1977; Whit-
 595 taker et al., 2007b, 2007a, 2008; Attal et al., 2011, 2008).

596 To calculate the height of the knickpoints, we manually pick the top and bottom
 597 of the knickpoint, using the onset and end of the trough in the calculated profile gradi-
 598 ent. We then fit a regression line through the upper and lower surface and calculate the
 599 elevation difference between these regression lines at the centre of the knickpoint. The
 600 location of the knickpoint is measured as the distance upstream from the scarp. The av-
 601 erage height of K_p1 (green stars, Figure 8b) was 12 ± 3 m on the Mua segment and 13 ± 3
 602 m on the Kasinje segment. Additional knickpoints (K_p2 and K_p3) were typically lower,
 603 measuring around 5 m on average; however, K_p2 on the southern Kasinje stream mea-
 604 sured 19 m in height, larger than the height of K_p1 measured along the stream (10 m).

605 The number of knickpoints corresponds well with number of sub-scarps identified
 606 on the scarp profiles, and confirms that more than one rupture event has likely occurred
 607 on both the Mua and Kasinje segments of the Bilila-Mtakataka (Figure 8b). The clus-
 608 tering of K_p1 suggests they were formed by the same event: the last rupture event (R1).
 609 Similarly, we attribute the similar distances of K_p2 on all profiles (Figure 12) to be due
 610 to a concurrent, or near concurrent, older rupture: the penultimate, observable surface
 611 rupturing event (R2). Along on the Naminkokwe and Mtuta rivers, which both have sim-
 612 ilar drainage areas (Figure 2), K_p3 are setback a similar distance. Furthermore, the knick-
 613 point of the Mtuta River is situated a few kilometres south of where a third rupture event
 614 was found on scarp profile K12. Consequently, this third knickpoint may be represen-
 615 tative of a potential third, older rupture (R3).



572 **Figure 11.** River and stream profiles for: a) Naminkokwe River; b) Mua north stream; c)
 573 Mua south stream; d) Livelezi River; e) Kasinje north stream; f) Kasinje south stream; and g)
 574 Mtuta River. Profile elevation (black circles) was filtered using the Savitzky-Golay digital filter
 575 and window size of 20 m. For the G_d plot a d of 10 (blue) and 70 m (red) were used to identify
 576 knickpoints. The dotted black line indicates a G_d of 0.2. Knickpoints identified in the gradient
 577 G_d profile are shown as grey triangles. These were then quality checked and considered tectonic
 578 knickpoints (green triangles) or artefacts of noise (orange triangles). Knickpoints are numbered
 579 K_p1 , K_p2 etc based on their distance from the scarp.



616 **Figure 12.** a) Knickpoint distance from scarp versus drainage area. b) Knickpoint distance
 617 from scarp versus scarp height. Filled symbols are knickpoints deemed to be tectonic knickpoints,
 618 whereas outlined symbols have been considered to be noise artefacts and have been removed from
 619 the analysis.

620 7 Discussion

621 7.1 Comparison between scarp and knickpoint analyses

622 Whereas previous analyses on the BMF have focused solely on the total scarp height
 623 (Hodge et al., 2018b, 2019), here using the high resolution DEM created from Pleiades
 624 data, we were able to identify sub-scarps and estimate the incremental vertical surface
 625 displacements. While it is possible that multiple splays were active during a single event,
 626 the consistent pattern of vertical displacements along the length of the segments sug-
 627 gests these sub-scarps record separate earthquakes rather than local variations in geom-
 628 etry. The average scarp height of the most recent rupture event (R1) was ~ 12 m on both
 629 segments. The penultimate rupture event (R2) identified from the composite and multi-
 630 scarps had a similar scarp height (~ 11 m). The R1 and R2 scarp height profiles show
 631 variability along the segments and there are significant gaps in where R2 was recorded
 632 due to noisy profiles. A third potential event recorded on K12 had a scarp height of 5
 633 m, and it is likely that any evidence for older events will have been obscured by erosion.
 634 The total scarp heights broadly match previous results (Hodge et al., 2018b, 2019), and
 635 show that while there is an intense local variability in the scarp height along the BMF,
 636 the average total scarp height is over 20 m on both segments, and is largest at the seg-
 637 ment centres (Figure 8).

638 The height of individual knickpoints that have formed during consecutive ruptures
 639 may be a proxy for the vertical offset in each earthquake (Wei et al., 2015). We com-
 640 pare the cumulative knickpoint height measured from each river profile to the total scarp
 641 height measured from the closest scarp profile and find that the river profiles on aver-
 642 age express 80% of the total scarp height. When comparing R1 knickpoint and scarp heights,
 643 the knickpoints record over 100% of the scarp height; as scarp height is locally variable,
 644 the closest scarp used here may not represent a larger scarp local to the knickpoint. The
 645 good correlation between knickpoint and scarp heights suggests that the well-defined first
 646 knickpoints (K1) are therefore likely true reflections of the latest vertical surface displace-
 647 ment from the most recent rupture on the two segments. The height of R2 from the river
 648 profiles is between 20% and 50% of the nearest R2 scarp height, when not including the
 649 abnormally large K2 height on the southern Kasinje stream. However, the nearest scarp

650 profiles were all composite scarps, which may comprise additional ruptures that have been
 651 masked. When compared the R2 knickpoint height to the closest R2 scarp height from
 652 multi-scarps, the knickpoints express between 55% and 80% of the vertical offset. The
 653 R3 knickpoint on the Mtuta River has a height that expresses 90% of the nearest R3 scarp
 654 height from a multi-scarp.

655 The abnormally large knickpoint height of second knickpoint (~ 19 m) on the south-
 656 ern Kasinje stream, when compared to other K_p2 heights (< 5 m) may be explained by
 657 a localised displacement high during an older event, or the inability to distinguish mul-
 658 tiple older ruptures. The nearest scarp profile was taken only a few hundred metres from
 659 the stream and shows evidence for an older rupture producing a ~ 16 m high scarp (Fig-
 660 ure 8). Because these profiles are from the centre of the Kasinje segment, this may im-
 661 ply that a larger displacement occurred here (conforming to a bell-shaped displacement
 662 profile); however, the large κt values from this region (Figure 10) may also suggest that
 663 older rupture markers may have been destroyed, and that the scarp and knickpoint R2
 664 may be formed from multiple, older events. In addition, the small discharge and catch-
 665 ment area for the southern Kasinje stream means that if a subsequent ruptures did oc-
 666 cur here, and did so within a short enough period of time, a break in the longitudinal
 667 profile between knickpoints may not have developed.

668 7.2 Age estimates

669 No historical rupture has been observed on the Bilila-Mtakataka fault, indicating
 670 that the most recent earthquake (R1) must have occurred over a hundred years ago (Midzi
 671 et al., 1999; Hodge et al., 2015). Our numerical model shows that even for regions with
 672 a small diffusion constant κ , a free face degrades and disappears within approximately
 673 a hundred years, consistent with our field and satellite observations. To remove individ-
 674 ual event markers on composite scarps required κt larger than 20 m^2 , corresponding to
 675 a total time since formation of at least two to four thousand years.

676 The estimated diffusion age of the Bilila Mtakataka scarp is $48 \pm 25 \text{ m}^2$, which cor-
 677 responds to a total time since formation of 6.4 ± 4.0 kyr, assuming a κ of $7.5 \pm 2.5 \text{ m}^2/\text{kyr}$.
 678 Assuming a constant κ for the entire scarp history may be invalid for regions where in-
 679 tense climatic variations occur over long timescales; however, drill cores from Lake Malawi
 680 suggest that the climatic conditions of Malawi have been relatively stable for the past
 681 70,000 years (Scholz et al., 2011). The range of estimates might therefore imply that sec-
 682 tions of the Mua and Kasinje segments are several thousand years older than others, and
 683 that the earlier earthquakes involved smaller segments rupturing independently. How-
 684 ever, there was no correlation between diffusion age and scarp height (Figure 10c), nor
 685 is the distribution of knickpoints and scarp heights representative of multiple discontin-
 686 uous ruptures. Instead we suggest that the wide variation in diffusion age is related to
 687 local erosional processes (i.e. variations in κ ; e.g. Kokkalas & Koukouvelas, 2005) includ-
 688 ing variations in properties of the fault damage zone associated with differences in the
 689 cross-cutting relationship between the scarp trend and the gneissic foliation (Hodge et
 690 al., 2018b).

691 The diffusion age for the Mua ($52 \pm 24 \text{ m}^2$) and Kasinje ($42 \pm 26 \text{ m}^2$) segments is
 692 the same within error, implying the scarps likely formed at similar points in time. Sim-
 693 ilarly, the consistent height of the R1 scarp implies that it formed in a single event across
 694 both segments. The fact that the R1 height does not decrease at the end of our study
 695 area suggests that it also propagated north onto the Mtakataka segment and south onto
 696 the Bilila segment. In contrast, the height of R2 scarp decreases at both the segment ends
 697 and the intersegment zone, suggesting separate ruptures of the Mua and Kasinje segments.
 698 Even ruptures ~ 20 km in length with 10 m of surface displacement would imply an un-
 699 usually large slip-length ratio (5×10^{-4}) compared to global catalogues (Scholz, 2002).
 700 We therefore suggest that the R2 event ruptured both segments concurrent - or near con-

701 current - in time, as supported by the similar diffusion ages. The lack of a displacement
 702 low between the segments from R1, as seen in R2, may suggest the segments have be-
 703 come more mature in their structural linkage over recent earthquake cycles. Our find-
 704 ings suggest therefore that the BMF segments, over the last two earthquake cycles, have
 705 not ruptured individually. This finding profoundly influences the seismic hazard of the
 706 area, as it implies that the rupture length is not constrained by the structural segment
 707 lengths (Goda et al., 2018).

708 7.3 Magnitude estimates

709 Using relationships between earthquake magnitude and the total average BMF scarp
 710 height (~ 14 m), previous studies had estimated that the scarp was formed by a M_W
 711 7.9 to 8.4 event (Jackson & Blenkinsop, 1997; Hodge et al., 2019). However, in this study
 712 we have concluded that the BMF scarp actually formed through multiple ruptures. As-
 713 suming that the whole BMF scarp reflects two earthquakes (i.e. any older events no longer
 714 contribute significantly to the scarp height), and that there was no vertical erosion be-
 715 tween these events, the average vertical displacement (i.e. throw) of each event is 7 ± 4
 716 m. In using these surface measurements to estimate average coseismic displacement \bar{D}_s
 717 we note that it has been practice to infer \bar{D}_s both directly from throw (i.e. scarp height;
 718 Schwartz & Coppersmith, 1984; DuRoss, 2008; Nicol et al., 2010) or from projecting throw
 719 into the fault dip (Villamor & Berryman, 2001; Xu et al., 2018; Litchfield et al., 2018).
 720 We apply both approaches here, noting that for a reasonable fault dip ($60^\circ \pm 5^\circ$), our
 721 projected estimates of \bar{D}_s are only slightly increased (8.1 ± 5.2 m).

722 Our new estimate of \bar{D}_s results in a slip-length ratio α of $6.8 \pm 5.5 \times 10^{-5}$ for a com-
 723 plete BMF rupture (rupture length, 110 km), which is in accordance with global values
 724 (Scholz, 2002). However, we cannot exclude the possibility that the most recent BMF
 725 earthquake ruptured only the Kasinje and Mua segments, in which case \bar{D}_s is 10 m, length
 726 ~ 40 km, and thus α is 2.5×10^{-4} . Applying the methodology of Jackson and Blenk-
 727 insop (1997) to calculate the magnitude of a complete BMF rupture, but with the re-
 728 visited value of \bar{D}_s , we calculate a range of magnitudes from M_W 7.7 to 8.3 (eq. 1, Ta-
 729 ble 1). Alternatively, we estimate the magnitude range for a complete BMF rupture of
 730 M_W 7.3 to 7.9 according to the \bar{D}_s -magnitude scaling law by Wells and Coppersmith
 731 (1994) (Table 1, eq. 2) and M_W 7.8 to 9.1 according to the \bar{D}_s -magnitude scaling laws
 732 for interplate dip-slip faults of Leonard (2010) (Table 1, eq. 3).

733 The Wells and Coppersmith (1994) magnitude estimates using \bar{D}_s are therefore com-
 734 parable to those estimated using their surface rupture length (L) scaling laws (Table 1,
 735 eq. 4), which range between M_W 7.4 and 7.5 assuming a complete BMF rupture. How-
 736 ever, the Leonard (2010) \bar{D}_s -magnitude scaling gives a larger M_W than the L -magnitude
 737 scaling (M_W 7.5, Table 1, eq. 5). This may be indicative of the fact that our estimates
 738 of α are either at the higher end of values proposed by Scholz (2002), or even greater;
 739 such high values of α have also been observed for other earthquakes, which like Malawi,
 740 are hosted in thick elastic crust (Rodgers & Little, 2006; Smekalin et al., 2010).

741 It is not possible to comment here further on which of the magnitude equations in
 742 Table 1 are most appropriate for the BMF, only to highlight the care that should be used
 743 when selecting earthquake scaling relationships (Stirling et al., 2013). Regardless, in ei-
 744 ther case, the estimated earthquake magnitude from a complete rupture of the BMF is
 745 slightly greater than the largest naturally recorded earthquake events on the EARS, the
 746 M_W 7.3 1910 Rukwa event (Ambraseys & Adams, 1991), the M_W 7.0 1990 Juba earth-
 747 quake (Hartnady, 2002), and the M_W 7 2006 Machaze earthquake (Fenton & Bommer,
 748 2006). Furthermore, the average M_W of 7.8 for a complete BMF rupture is slightly lower
 749 than previously estimated (Jackson & Blenkinsop, 1997) and is another example of where
 750 better constraining rupture slip has led to lower magnitude estimates (e.g., the 1739 Yinchuan
 751 earthquake, China; Middleton et al., 2016).

762 **Table 1.** Earthquake magnitude (including lower and upper) estimates using $L = 110$ km (± 2
763 km), $\bar{D}_s = 7$ m (± 4 m), $G = 30$ GPa (± 5 GPa, Stein and Liu (2009)), and $W = T_s/\delta$ (where
764 seismogenic thickness $T_s = 30$ km ± 5 km Jackson and Blenkinsop (1993), and dip $\delta = 60^\circ \pm 5^\circ$).
765 ^[1] Jackson and Blenkinsop (1997). ^[2] Hanks and Kanamori (1979). ^[3] Wells and Coppersmith
766 (1994). ^[4] Leonard (2010)

Eq N ^o	Description	Equation	Average M _W	M _W Range
(1)	Normal fault slip ^{[1][2]}	$M_W = \frac{2}{3} \cdot \log(G\bar{D}_sLW) - 6.05$	8.0	7.7 - 8.3
(2)	All slip type ^[3]	$M_W = 6.93 + 0.82 \cdot \log(\bar{D}_s)$	7.6	7.3 - 7.9
(3)	Interplate dip-slip ^[4]	$M_W = 6.84 + 2.00 \cdot \log(\bar{D}_s)$	8.5	7.8 - 9.1
(4)	All slip type ^[3]	$M_W = 5.08 + 1.16 \cdot \log(L)$	7.5	7.4 - 7.5
(5)	Interplate dip-slip ^[4]	$M_W = 4.40 + 1.52 \cdot \log(L)$	7.5	7.5

752 These calculations assume a characteristic earthquake model for the BMF, and whilst
753 the geomorphological analysis in this study found no evidence for single segment rup-
754 tures along the Mua and Kasinje segments, multi-segment ruptures may occur across both
755 segments but not the entire fault. For example, the Citsulo segment may be a barrier
756 to rupture propagation (Hodge et al., 2018b). Such ruptures would have a lower earth-
757 quake magnitude, due to the shorter rupture length, but also have a shorter recurrence
758 interval. Complete and segmented ruptures along the BMF pose different seismic haz-
759 ards for the region (Hodge et al., 2015; Goda et al., 2018). A detailed geomorphologi-
760 cal analysis on the remaining BMF segments (Ngodzi, Mtakataka, Citsulo and Bilila)
761 is therefore required.

767 8 Conclusion

768 The ~ 110 km long Bilila-Mtakataka fault comprises a scarp whose average height
769 (~ 14 m) exceeds that which would have formed from a single event, given global slip-
770 length scaling laws (e.g. Scholz, 2002). Indeed, the two central structural segments - the
771 Mua and Kasinje segments - have scarps more than 20 m high in places. Previous work
772 has suggested that scarps of similar heights form through multiple ruptures on the same
773 fault plane (a composite scarp) or unique near-surface fault planes (a multi-scarp). Our
774 numerical models of scarp diffusion show that multi-scarps and composite-scarps display
775 differing morphological signatures.

776 By undertaking a geomorphological analysis of the fault scarps along the Mua and
777 Kasinje segments, using a high resolution DEM, we suggest there is evidence for at least
778 two ruptures. A separate knickpoint analysis on three rivers and four streams that cross
779 the fault scarp agree with these findings. By calculating the individual vertical displace-
780 ment of each rupture from the scarp and knickpoints, we estimate the average vertical
781 surface displacement along the two segments to be ~ 10 m per rupture. Results from
782 a scarp degradation model used to estimate diffusion age κt on each scarp profile, by find-
783 ing a best fit to the current profile, imply that the most recent rupture was continuous
784 across both structural segments, and that the penultimate rupture was concurrent, or
785 near-concurrent, in time across both segments. Extrapolating these findings for the en-

786 tire BMF, we suggest that the surface slip per event is less than 10 m, as expected by
 787 global slip-length scaling laws, and that a complete rupture would equate to a M_W range
 788 of 7.5 to 8.1. This is likely smaller than previously suggested for the fault, but greater
 789 than the largest earthquakes recorded along the entire EARS. We have demonstrated
 790 that high resolution satellite topography can be used to identify surface ruptures from
 791 multiple earthquakes. This could be applied to other large, prehistoric normal fault scarps
 792 whose scarp height exceeds what would be anticipated by a single earthquake event (Scholz,
 793 2002). Candidates for this include the Kanda fault, Lake Rukwa (Vittori et al., 1997;
 794 Macheyeke et al., 2007), the Nahef East fault, northern Israel (Mitchell et al., 2001), the
 795 Wasatch fault zone faults, Utah (Swan et al., 1980; DuRoss et al., 2015) and the Dixie
 796 Valley-Pleasant Valley faults (Zhang et al., 1991).

797 Acknowledgments

798 Michael Hodge is supported by the NERC GW4+ Doctoral Training Partnership (grant
 799 code NE/L002434/1) and Centre for Observation and Modelling of Earthquakes, Vol-
 800 canoes and Tectonics (COMET). Juliet Biggs is supported by COMET and the NERC
 801 Large Grant Looking into Continents from Space (LiCS, NE/K010913/1). Juliet Biggs,
 802 Åke Fagereng, Luke Wedmore and Jack Williams are supported by the EPSRC Global
 803 Challenges grant PREPARE (EP/P028233/1). Hassan Mdala acknowledges the Geolog-
 804 ical Survey Department, Malawi, for attaching him to the project. All authors acknowl-
 805 edge the Geological Survey Department, Malawi, for their assistance with fieldwork in
 806 Malawi. Pleiades data were obtained using a small grant from COMET and the point
 807 cloud data are available from opentopography.org: <https://doi.org/10.5069/G92R3PSV>
 808 (Mua section) and <https://doi.org/10.5069/G96H4FJ1> (Kasinje section). We thank Dan
 809 Hobley and two anonymous reviewers for their helpful comments on drafts of this manuscript.

810 References

- 811 Ambraseys, N., & Adams, R. (1991). Reappraisal of major African earthquakes,
 812 south of 20 N, 1900–1930. *Natural Hazards*, *4*, 389–419. Retrieved from
 813 <http://link.springer.com/article/10.1007/BF00126646>
- 814 Anders, M. H., & Schlische, R. W. (1994, mar). Overlapping Faults, Intrabasin
 815 Highs, and the Growth of Normal Faults. *The Journal of Geology*, *102*(2),
 816 165–179. Retrieved from [http://www.journals.uchicago.edu/doi/abs/](http://www.journals.uchicago.edu/doi/abs/10.1086/629661)
 817 [10.1086/629661](http://www.journals.uchicago.edu/doi/abs/10.1086/629661) doi: 10.1086/629661
- 818 Andrews, D. J., & Hanks, T. C. (1985). Scarp Degraded by Linear Diffusion: Inverse
 819 Solution for Age. *Journal of Geophysical Research*, *90*(B12), 10193–10208.
- 820 Arrowsmith, J. R., Pollard, D. D., & Rhodes, D. D. (1996). Hillslope development
 821 in areas of active tectonics. *Journal of Geophysical Research*, *101*(B3), 6255–
 822 6275. doi: 10.1029/95JB02583
- 823 Arrowsmith, J. R., Rhodes, D. D., & Pollard, D. D. (1998). Morphologic dating
 824 of scarps formed by repeated slip events along the San Andreas Fault, Car-
 825 rizo Plain, California. *Journal of Geophysical Research Solid Earth*, *103*(B5),
 826 10141–10160.
- 827 Attal, M., Cowie, P. A., Whittaker, A. C., Hobley, D., Tucker, G. E., & Roberts,
 828 G. P. (2011). Testing fluvial erosion models using the transient response of
 829 bedrock rivers to tectonic forcing in the Apennines, Italy. *Journal of Geophysi-
 830 cal Research: Earth Surface*, *116*(2), 1–17. doi: 10.1029/2010JF001875
- 831 Attal, M., Tucker, G. E., Whittaker, A. C., Cowie, P. A., & Roberts, G. P. (2008).
 832 Modelling fluvial incision and transient landscape evolution: Influence of dy-
 833 namic Channel adjustment. *Journal of Geophysical Research: Earth Surface*,
 834 *113*(3), 1–16. doi: 10.1029/2007JF000893
- 835 Avouac, J.-p. (1993). Analysis of Scarp Profiles: Evaluation of Errors in Morpho-
 836 logic Dating. *Journal of Geophysical Research*, *98*(B4), 6745–6754.

- 837 Avouac, J.-p., & Peltzer, G. (1993). Active Tectonics in Southern Xinjiang , China
838 : Analysis of Terrace Riser and Normal Fault Scarp Degradation Along the
839 Hotan-Qira Fault System. *Journal of Geophysical Research*, 98(B12), 21,773–
840 21,807.
- 841 Berlin, M. M., & Anderson, R. S. (2007). Modeling of knickpoint retreat on the
842 Roan Plateau, western Colorado. *Journal of Geophysical Research: Earth Sur-
843 face*, 112(3), 1–16. doi: 10.1029/2006JF000553
- 844 Bishop, P., Hoey, T. B., Jansen, J. D., & Lexartza Artza, I. (2005). Knickpoint
845 recession rate and catchment area: The case of uplifted rivers in Eastern
846 Scotland. *Earth Surface Processes and Landforms*, 30(6), 767–778. doi:
847 10.1002/esp.1191
- 848 Bucknam, R. C., & Anderson, R. E. (1979). Estimation of fault-scarp ages from a
849 scarp-height-slope-angle relationship. *Geology*, 7, 11–14.
- 850 Burbank, D. W., & Anderson, R. S. (2011). *Tectonic geomorphology*. John Wiley &
851 Sons.
- 852 Carretier, S., Ritz, J. F., Jackson, J., & Bayasgalan, A. (2002). Morphological dat-
853 ing of cumulative reverse fault scarps: Examples from the Gurvan Bogd fault
854 system, Mongolia. *Geophysical Journal International*, 148(2), 256–277. doi:
855 10.1046/j.1365-246X.2002.01599.x
- 856 Castillo, M. (2017). Landscape evolution of the graben of Puerto Vallarta
857 (west-central Mexico) using the analysis of landforms and stream long
858 profiles. *Journal of South American Earth Sciences*, 73, 10–21. Re-
859 trieved from <http://dx.doi.org/10.1016/j.jsames.2016.11.002> doi:
860 10.1016/j.jsames.2016.11.002
- 861 Cleveland, W. S. (1981). LOWESS: A program for smoothing scatterplots by robust
862 locally weighted regression. *The American Statistician*, 35(1), 54.
- 863 Commins, D., Gupta, S., & Cartwright, J. A. (2005). Deformed streams reveal
864 growth and linkage of a normal fault array in the Deformed streams reveal
865 growth and linkage of a normal fault array in the Canyonlands graben , Utah.
866 *Geology*, 33(8), 645–648. doi: 10.1130/G21433.1
- 867 Cowie, P. A., Attal, M., Tucker, G. E., Whittaker, A. C., Naylor, M., Ganas, A.,
868 & Roberts, G. P. (2006). Investigating the surface process response to fault
869 interaction and linkage using a numerical modelling approach. *Basin Research*,
870 18(3), 231–266. doi: 10.1111/j.1365-2117.2006.00298.x
- 871 Crone, A. J., & Haller, K. M. (1991). Segmentation and the coseismic behavior of
872 Basin and Range normal faults: examples from east-central Idaho and south-
873 western Montana, U.S.A. *Journal of Structural Geology*, 13(2), 151–164.
874 Retrieved from [http://www.sciencedirect.com/science/article/pii/
875 0191814191900630](http://www.sciencedirect.com/science/article/pii/0191814191900630) doi: [http://dx.doi.org/10.1016/0191-8141\(91\)90063-0](http://dx.doi.org/10.1016/0191-8141(91)90063-0)
- 876 Crosby, B. T., & Whipple, K. X. (2006). Knickpoint initiation and distribu-
877 tion within fluvial networks: 236 waterfalls in the Waipaoa River, North
878 Island, New Zealand. *Geomorphology*, 82(1-2), 16–38. doi: 10.1016/
879 j.geomorph.2005.08.023
- 880 Culling, W. E. H. (1963). Soil creep and the development of hillside slopes. *The
881 Journal of Geology*, 71(2), 127–161.
- 882 Dawson, A., & Kirkpatrick, I. (1968). The geology of the Cape Maclear peninsula
883 and Lower Bwanje valley. *Bulletin of the Geological Survey, Malawi*, 28(71).
- 884 Duffy, O. B., Brocklehurst, S. H., Gawthorpe, R. L., Leeder, M. R., & Finch, E.
885 (2014). Controls on landscape and drainage evolution in regions of distributed
886 normal faulting: Perachora Peninsula, Corinth Rift, Central Greece. *Basin
887 Research*, 27, 1–22. doi: 10.1111/bre.12084
- 888 Dulanya, Z. (2017). A review of the geomorphotectonic evolution of the south
889 malawi rift. *Journal of African Earth Sciences*, 129, 728–738.
- 890 DuRoss, C. B. (2008). Holocene vertical displacement on the central segments of
891 the Wasatch fault zone, Utah. *Bulletin of the Seismological Society of Amer-*

- 892 ica, 98(6), 2918–2933. doi: 10.1785/0120080119
- 893 DuRoss, C. B., Personius, S. F., Crone, A. J., Olig, S. S., Hylland, M. D., Lund,
894 W. R., & Schwartz, D. P. (2015). Fault segmentation: New concepts from the
895 Wasatch Fault Zone, Utah, USA. *Journal of Geophysical Research:Solid Earth*,
896 121, 1131–1157. doi: 10.1002/2015JB012419.Received
- 897 Ebinger, C. (1989). Tectonic development of the western branch of the East African
898 rift system. *Geological Society of America Bulletin*, 101, 885–903. Retrieved
899 from <http://gsabulletin.gsapubs.org/content/101/7/885.short> doi: 10
900 .1130/0016-7606(1989)101(0885
- 901 Ebinger, C., Rosendahl, B., & Reynolds, D. (1987). Tectonic model of the
902 Malawi rift, Africa. *Tectonophysics*, 141, 215–235. Retrieved from
903 <http://www.sciencedirect.com/science/article/pii/0040195187901879>
- 904 Elvidge, C., & Lyon, R. (1985). Estimate of the vegetation contribution to the
905 1.65/2.22 m ratio in airborne thematic-mapper imagery of the Virginia Range,
906 Nevada. *International Journal of Remote Sensing*, 6, 75–88.
- 907 Ewiak, O., Victor, P., & Oncken, O. (2015). Investigating multiple fault rupture at
908 the Salar del Carmen segment of the Atacama Fault System (northern Chile):
909 Fault scarp morphology and knickpoint analysis. *Tectonics*, 34(2), 187–212.
910 doi: 10.1002/2014TC003599
- 911 Fenton, C. H., & Bommer, J. J. (2006). The Mw7 Machaze, Mozambique, earth-
912 quake of 23 February 2006. *Seismological Research Letters*, 77(4), 426–439.
- 913 Finlayson, D. P., Montgomery, D. R., & Hallet, B. (2002). Spatial coincidence of
914 rapid inferred erosion with young metamorphic massifs in the Himalayas. *Ge-
915 ology*, 30(3), 219–222. doi: 10.1130/0091-7613(2002)030(0219:SCORIE)2.0.CO;
916 2
- 917 Flannery, J., & Rosendahl, B. (1990). The seismic stratigraphy of Lake Malawi,
918 Africa: implications for interpreting geological processes in lacustrine
919 rifts. *Journal of African Earth Sciences*, 10(3), 519–548. Retrieved from
920 <http://www.sciencedirect.com/science/article/pii/089953629090104M>
- 921 Fu, B., Ninomiya, Y., Lei, X., Toda, S., & Awata, Y. (2004). Mapping active
922 fault associated with the 2003 Mw 6.6 Bam (SE Iran) earthquake with
923 ASTER 3D images. *Remote Sensing of Environment*, 92, 153–157. doi:
924 10.1016/j.rse.2004.05.019
- 925 Ganas, A., Pavlides, S., & Karastathis, V. (2005). DEM-based morphome-
926 try of range-front escarpments in Attica , central Greece , and its relation
927 to fault slip rates. *Geomorphology*, 65(September 2004), 301–319. doi:
928 10.1016/j.geomorph.2004.09.006
- 929 Gasparini, N. M., Bras, R. L., & Whipple, K. X. (2006). Numerical modeling of
930 non-steady river profile evolution using a sediment-flux-dependent incision
931 model. *Geological Society of America Special Paper*, 398(08), 127–141. doi:
932 10.1130/2006.2398(08).
- 933 Giba, M., Walsh, J., & Nicol, A. (2012, jun). Segmentation and growth of an
934 obliquely reactivated normal fault. *Journal of Structural Geology*, 39, 253–
935 267. Retrieved from [http://linkinghub.elsevier.com/retrieve/pii/
936 S0191814112000132](http://linkinghub.elsevier.com/retrieve/pii/S0191814112000132) doi: 10.1016/j.jsg.2012.01.004
- 937 Goda, K., Kloukinas, P., Risi, R., Hodge, M., Kafodya, I., Ngoma, I., ... Macdon-
938 ald, J. (2018, jun). Scenario-based seismic risk assessment for Malawi using
939 improved information on earthquake sources and local building characteristics.
940 In *16th european conference on earthquake engineering*.
- 941 Gomberg, J., Reasenber, P. a., Bodin, P., & Harris, R. a. (2001). Earthquake trig-
942 gering by seismic waves following the Landers and Hector Mine earthquakes.
943 *Nature*, 411(6836), 462–466. doi: 10.1038/35078053
- 944 Grigillo, D., Frasn, M. K., & Petrovič, D. (2012). Automated building extraction from
945 IKONOS images in suburban areas. *International Journal of Remote Sensing*,
946 33(16), 5149–5170. doi: 10.1080/01431161.2012.659356

- 947 Hanks, T. C., Bucknam, R. C., Lajoie, K. R., & Wallace, R. E. (1984). Modifica-
 948 tion of Wave-Cut and Faulting-Controlled Landforms. *Journal of Geophysical*
 949 *Research*, *89*(10), 5771–5790. doi: 10.1029/JB089iB07p05771
- 950 Hanks, T. C., & Kanamori, H. (1979). A moment magnitude scale. *Journal of Geo-*
 951 *physical Research*, *84*(B5), 2348–2350.
- 952 Hartnady, C. (2002). Earthquake hazard in Africa: perspectives on the
 953 Nubia-Somalia boundary: news and view. *South African journal of sci-*
 954 *ence*, *98*, 425–428. Retrieved from [http://reference.sabinet.co.za/](http://reference.sabinet.co.za/sa{_}epublication{_}article/sajsci{_}v98{_}n9{_}10{_}a5)
 955 [sa{_}epublication{_}article/sajsci{_}v98{_}n9{_}10{_}a5](http://reference.sabinet.co.za/sa{_}epublication{_}article/sajsci{_}v98{_}n9{_}10{_}a5)
- 956 Hayakawa, Y. S., & Oguchi, T. (2006). DEM-based identification of fluvial knick-
 957 zones and its application to Japanese mountain rivers. *Geomorphology*, *78*, 90–
 958 106. doi: 10.1016/j.geomorph.2006.01.018
- 959 Hayakawa, Y. S., & Oguchi, T. (2009). GIS analysis of fluvial knickzone distribu-
 960 tion in Japanese mountain watersheds. *Geomorphology*, *111*, 27–37. Retrieved
 961 from <http://dx.doi.org/10.1016/j.geomorph.2007.11.016> doi: 10.1016/j.
 962 [geomorph.2007.11.016](http://dx.doi.org/10.1016/j.geomorph.2007.11.016)
- 963 He, Z., & Ma, B. (2015). Holocene paleoearthquakes of the Daqingshan fault de-
 964 tected from knickpoint identification and alluvial soil profile. *Journal of Asian*
 965 *Earth Sciences*, *98*, 261–271. Retrieved from [http://dx.doi.org/10.1016/j.](http://dx.doi.org/10.1016/j.jseaes.2014.11.025)
 966 [jseaes.2014.11.025](http://dx.doi.org/10.1016/j.jseaes.2014.11.025) doi: 10.1016/j.jseaes.2014.11.025
- 967 Hodge, M., Biggs, J., Fagereng, Å., Elliott, A., Mdala, H., & Mphepo, F. (2019). A
 968 semi-automated algorithm to quantify scarp morphology (sparta): application
 969 to normal faults in southern malawi. *Solid Earth*, *10*(1), 27–57.
- 970 Hodge, M., Biggs, J., Fagereng, A., & Mdala, H. (2018b). Controls on early-rift ge-
 971 ometry: new perspectives from the Bilila-Mtakataka fault, Malawi. *Geophysical*
 972 *Research Letters*, *45*(9), 3896–3905.
- 973 Hodge, M., Biggs, J., Goda, K., & Aspinall, W. (2015). Assessing infrequent large
 974 earthquakes using geomorphology and geodesy: the Malawi Rift. *Natural Haz-*
 975 *ards*, *76*(3), 1781–1806. Retrieved from [http://dx.doi.org/10.1007/s11069-](http://dx.doi.org/10.1007/s11069-014-1572-y)
 976 [-014-1572-y](http://dx.doi.org/10.1007/s11069-014-1572-y) doi: 10.1007/s11069-014-1572-y
- 977 Hodge, M., Fagereng, A., & Biggs, J. (2018a). The role of static stress changes
 978 during earthquakes in linking normal faults: bend, growth, breached ramp or
 979 transform? *Journal of Geophysical Research: Solid Earth*, *123*, 797–814.
- 980 Holbrook, J., & Schumm, S. A. (1999). Geomorphic and sedimentary response
 981 of rivers to tectonic deformation: A brief review and critique of a tool for
 982 recognizing subtle epeirogenic deformation in modern and ancient settings.
 983 *Tectonophysics*, *305*(1–3), 287–306. doi: 10.1016/S0040-1951(99)00011-6
- 984 Holland, W. N., & Pickup, G. (1976). Flume study of knickpoint development in
 985 stratified sediment. *Bulletin of the Geological Society of America*, *87*(1), 76–
 986 82. doi: 10.1130/0016-7606(1976)87<76:FSOKDI>2.0.CO;2
- 987 Howard, A. D., & Kerby, G. (1983). Channel changes in badlands. *Geological Soci-*
 988 *ety of America Bulletin*, *94*(6), 739–752. doi: 10.1130/0016-7606(1983)94<739:
 989 [CCIB>2.0.CO;2](http://dx.doi.org/10.1130/0016-7606(1983)94<739:CCIB>2.0.CO;2)
- 990 Jackson, J., & Blenkinsop, T. (1993). The Malawi earthquake of March 10, 1989:
 991 Deep faulting within the East Africa Rift System. *Tectonics*, *12*(5), 1131–
 992 1139.
- 993 Jackson, J., & Blenkinsop, T. (1997). The Bilila-Mtakataka fault in Malawi: An ac-
 994 tive, 100-km long, normal fault segment in thick seismogenic crust. *Tectonics*,
 995 *16*(1), 137–150.
- 996 Kokkalas, S., & Koukouvelas, I. K. (2005). Fault-scarp degradation modeling in cen-
 997 tral Greece: The Kaparelli and Eliki faults (Gulf of Corinth) as a case study.
 998 *Journal of Geodynamics*, *40*(2–3), 200–215. doi: 10.1016/j.jog.2005.07.006
- 999 Kristensen, M. B., Childs, C. J., & Korstgard, J. A. (2008). The 3D geometry of
 1000 small-scale relay zones between normal faults in soft sediments. *Journal of*
 1001 *Structural Geology*, *30*(2), 257–272. doi: 10.1016/j.jsg.2007.11.003

- 1002 Laó-Dávila, D. A., Al-Salmi, H. S., Abdelsalam, M. G., & Atekwana, E. A. (2015).
 1003 Hierarchical segmentation of the Malawi Rift: The influence of inherited litho-
 1004 spheric heterogeneity and kinematics in the evolution of continental rifts.
 1005 *Tectonics*, *34*, 2399–2417. Retrieved from [http://doi.wiley.com/10.1002/](http://doi.wiley.com/10.1002/2015TC003953)
 1006 [2015TC003953](http://doi.wiley.com/10.1002/2015TC003953) doi: 10.1002/2015TC003953
- 1007 Lee, J.-c., Chu, H.-t., Angelier, J., Chan, Y.-c., Hu, J.-c., Lu, C.-y., & Rau, R.-j.
 1008 (2002). Geometry and structure of northern surface ruptures of the 1999 Mw
 1009 7.6 Chi-Chi Taiwan earthquake : influence from inherited fold belt structures.
 1010 *Journal of Structural Geology*, *24*, 173–192.
- 1011 Leonard, M. (2010, oct). Earthquake Fault Scaling: Self-Consistent Relating of
 1012 Rupture Length, Width, Average Displacement, and Moment Release. *Bul-*
 1013 *letin of the Seismological Society of America*, *100*(5A), 1971–1988. Retrieved
 1014 from <http://www.bssaonline.org/content/100/5A/1971.abstract> doi:
 1015 10.1785/0120090189
- 1016 Leopold, L. B., & Maddock, T. (1953). *The hydraulic geometry of stream channels*
 1017 *and some physiographic implications* (Vol. 252). US Government Printing Of-
 1018 fice.
- 1019 Lin, A., Sano, M., Wang, M., Yan, B., Bian, D., Fueta, R., & Hosoya, T. (2017).
 1020 Paleoseismic study of the Kamishiro Fault on the northern segment of the
 1021 Itoigawa–Shizuoka Tectonic Line, Japan. *Journal of Seismology*, *21*(4), 683–
 1022 703. doi: 10.1007/s10950-016-9629-x
- 1023 Litchfield, N. J., Campbell, J. K., & Nicol, A. (2003). Recognition of active reverse
 1024 faults and folds in north canterbury, new zealand, using structural mapping
 1025 and geomorphic analysis. *New Zealand Journal of Geology and Geophysics*,
 1026 *46*(4), 563–579.
- 1027 Litchfield, N. J., Villamor, P., van Dissen, R. J., Nicol, A., Barnes, P. M., Barrell,
 1028 D. J., . . . Zinke, R. (2018). Surface rupture of multiple crustal faults in the
 1029 2016 Mw7.8 Kaikōura, New Zealand, earthquake. *Bulletin of the Seismological*
 1030 *Society of America*, *108*(3B), 1496–1520. doi: 10.1785/0120170300
- 1031 Macheyeke, A. S., Delvaux, D., Kervyn, F., Petermans, T., & Verbeeck, K. (2007).
 1032 Occurrence of large earthquakes along the major Kanda fault system
 1033 (Tanganyika-Rukwa rift, SW highlands of Tanzania). *Geophysical Research*
 1034 *Abstracts*, *9*, 9–10.
- 1035 Mackenzie, D., & Elliott, A. (2017). Untangling tectonic slip from the potentially
 1036 misleading effects of landform geometry. *Geosphere*, *13*(4), 1310–1328. doi: 10
 1037 .1130/GES01386.1
- 1038 Manighetti, I., Campillo, M., Sammis, C., Mai, P. M., & King, G. (2005). Evidence
 1039 for self-similar, triangular slip distributions on earthquakes: Implications for
 1040 earthquake and fault mechanics. *Journal of Geophysical Research B: Solid*
 1041 *Earth*, *110*(5), 1–25. doi: 10.1029/2004JB003174
- 1042 Manighetti, I., King, G. C. P., & Gaudemer, Y. (2001). Slip accumulation and
 1043 lateral propagation of active normal faults in Afar. *Journal of Geophysical Re-*
 1044 *search*, *106*(B7), 13,667–13,696.
- 1045 Mayer, L. (1982). *Quantitative Tectonic Geomorphology with Applications to Neo-*
 1046 *tectonics of Northwestern Arizona* (Doctoral dissertation, The University of
 1047 Arizona). Retrieved from <http://hdl.handle.net/10150/187532>
- 1048 McCaLpin, J. P. (2009). *Paleoseismology* (Vol. 95). Academic press.
- 1049 Michetti, M., & Brunamonte, F. (1996). Trench investigations of the 1915 Fucino
 1050 earthquake fault scarps (Abruzzo, central Italy): Geological evidence of large
 1051 historical events. *Journal of Geophysical Research*, *101*, 5921–5936.
- 1052 Middleton, T. A., Walker, R. T., Parsons, B., Lei, Q., Zhou, Y., & Ren, Z. (2016).
 1053 A major, intraplate, normal-faulting earthquake: The 1739 Yinchuan event
 1054 in northern China. *Journal of Geophysical Research B: Solid Earth*, *121*(1),
 1055 293–320. doi: 10.1002/2015JB012355
- 1056 Midzi, V., Hlatywago, D. J., Chapola, L. S., Kebede, F., Atakan, K., Lombe, D. K.,

- 1057 ... Tugume, F. A. (1999). Seismic hazard assessment in Eastern and Southern
1058 Africa. *Annali Di Geofisica*, *42*(6), 1067–1083.
- 1059 Mitchell, S. G., Matmon, A., Bierman, R., Enzel, Y., Caffee, M., & Rizzo, D. (2001).
1060 Displacement history of a limestone normal fault scarp, northern Israel, from
1061 cosmogenic ^{36}Cl . *Journal of Geophysical Research*, *106*, 4247–4264.
- 1062 Montgomery, D. R., & Brandon, M. T. (2002). Topographic controls on erosion
1063 rates in tectonically active mountain ranges. *Earth and Planetary Science Let-*
1064 *ters*, *201*(3-4), 481–489. doi: 10.1016/S0012-821X(02)00725-2
- 1065 Morewood, N. C., & Roberts, G. P. (2001). Comparison of surface slip and fo-
1066 cal mechanism slip data along normal faults: An example from the eastern
1067 Gulf of Corinth, Greece. *Journal of Structural Geology*, *23*, 473–487. doi:
1068 10.1016/S0191-8141(00)00126-7
- 1069 Mueller, K. J., & Rockwell, T. K. (1995). Late Quaternary activity of the Laguna
1070 Salada fault in northern Baja California, Mexico. *Geological Society of Amer-*
1071 *ica Bulletin*, *107*(1), 8–18. doi: 10.1130/0016-7606(1995)107(0008:LQAOTL)2
1072 .3.CO;2
- 1073 Nash, D. B. (1980). Morphologic dating of degraded normal fault scarps. *The Jour-*
1074 *nal of Geology*, *88*(3), 353–360.
- 1075 Nash, D. B. (1984). Morphologic dating of fluvial terrace scarps and fault scarps
1076 near West Yellowstone, Montana. *Geological Society of America Bulletin*,
1077 *95*(12), 1413–1424. doi: 10.1130/0016-7606(1984)95(1413:MDOFTS)2.0.CO;2
- 1078 Nicol, A., Walsh, J., Villamor, P., Seebeck, H., & Berryman, K. (2010, aug). Nor-
1079 mal fault interactions, paleoearthquakes and growth in an active rift. *Journal*
1080 *of Structural Geology*, *32*(8), 1101–1113. Retrieved from [http://linkinghub](http://linkinghub.elsevier.com/retrieve/pii/S0191814110001100)
1081 [.elsevier.com/retrieve/pii/S0191814110001100](http://linkinghub.elsevier.com/retrieve/pii/S0191814110001100) doi: 10.1016/j.jsg.2010
1082 .06.018
- 1083 Nivière, B., & Marquis, G. (2000). Evolution of terrace risers along the upper Rhine
1084 graben inferred from morphologic dating methods: Evidence of climatic and
1085 tectonic forcing. *Geophysical Journal International*, *141*(3), 577–594. doi:
1086 10.1046/j.1365-246X.2000.00123.x
- 1087 Ouchi, S. (1985). Response of Alluvial Rivers to Slow Active Tectonic Move-
1088 ment. *Geological Society of America Bulletin*, *96*, 504–515. doi: 10.1130/
1089 0016-7606(1985)96(504:ROARTS)2.0.CO;2
- 1090 Palyvos, N., Pantosti, D., De Martini, P. M., Lemeille, F., Sorel, D., & Pavlopoulos,
1091 K. (2005). The Aigion-Neos Erineos coastal normal fault system (western
1092 Corinth Gulf Rift, Greece): Geomorphological signature, recent earthquake his-
1093 tory, and evolution. *Journal of Geophysical Research B: Solid Earth*, *110*(9),
1094 1–15. doi: 10.1029/2004JB003165
- 1095 Perrin, C., Manighetti, I., Ampuero, J.-p., Cappa, F., & Gaudemer, Y. (2016a).
1096 Location of largest earthquake slip and fast rupture controlled by along-strike
1097 change in fault structural maturity due to fault growth. *Journal of Geophysical*
1098 *Research: Solid Earth*, *121*, 3666–3685. doi: 10.1002/2015JB012671. Received
- 1099 Perrin, C., Manighetti, I., & Gaudemer, Y. (2016b). Off-fault tip splay networks :
1100 A genetic and generic property of faults indicative of their long-term propaga-
1101 tion. *Comptes Rendus Geoscience*, *348*, 52–60.
- 1102 Peters, G., & van Balen, R. T. (2007). Tectonic geomorphology of the northern Up-
1103 per Rhine Graben, Germany. *Global and Planetary Change*, *58*, 310–334. doi:
1104 10.1016/j.gloplacha.2006.11.041
- 1105 Philippon, M., Willingshofer, E., Sokoutis, D., Corti, G., Sani, F., Bonini, M., ...
1106 Pira, V. G. L. (2015). Slip re-orientation in oblique rifts. *Geology*, *43*(2), 1–4.
1107 doi: 10.1130/G36208.1
- 1108 Rawat, J. S., & Joshi, R. C. (2012). Remote-sensing and GIS-based landslide-
1109 susceptibility zonation using the landslide index method in Igo River Basin,
1110 Eastern Himalaya, India. *International Journal of Remote Sensing*, *33*(12),
1111 3751–3767. doi: 10.1080/01431161.2011.633121

- 1112 Rodgers, D. W., & Little, T. A. (2006). World's largest coseismic strike-slip offset:
 1113 The 1855 rupture of the Wairarapa Fault, New Zealand, and implications for
 1114 displacement/length scaling of continental earthquakes. *Journal of Geophysical*
 1115 *Research: Solid Earth*, *111*(12), 1–19. doi: 10.1029/2005JB004065
- 1116 Rosenbloom, N. A., & Anderson, R. S. (1994). Hillslope and channel evolution in
 1117 a marine terraced landscape, Santa Cruz, California Abstract. A flight of
 1118 marine terraces along California coastline provides a unique posits m tall de-
 1119 caying sea become rounded of the Five bedrock sueam channels to th. *Journal*
 1120 *of Geophysical Research*, *99*(94), 13–14. doi: 10.1029/94JB00048
- 1121 Saria, E., Calais, E., Stamps, D. S., Delvaux, D., & Hartnady, C. J. H. (2014). Jour-
 1122 nal of Geophysical Research : Solid Earth Present-day kinematics of the East
 1123 African Rift. *Journal of Geophysical Research: Solid Earth*, *119*, 3584–3600.
 1124 doi: 10.1002/2013JB010901.Received
- 1125 Savitzky, A., & Golay, M. J. (1964). Smoothing and Differentiation of Data by Sim-
 1126 plified Least Squares Procedures. *Analytical Chemistry*, *36*(8), 1627–1639. doi:
 1127 10.1021/ac60214a047
- 1128 Scholz, C. (2002). *The mechanics of earthquakes and faulting*. Cambridge university
 1129 press.
- 1130 Scholz, C., Cohen, A. S., Johnson, T. C., King, J., Talbot, M. R., & Brown, E. T.
 1131 (2011). Scientific drilling in the Great Rift Valley: The 2005 Lake Malawi
 1132 Scientific Drilling Project - An overview of the past 145,000years of climate
 1133 variability in Southern Hemisphere East Africa. *Palaeogeography, Palaeocli-*
 1134 *matology, Palaeoecology*, *303*(1-4), 3–19. Retrieved from [http://dx.doi.org/](http://dx.doi.org/10.1016/j.palaeo.2010.10.030)
 1135 [10.1016/j.palaeo.2010.10.030](http://dx.doi.org/10.1016/j.palaeo.2010.10.030) doi: 10.1016/j.palaeo.2010.10.030
- 1136 Schwartz, D. P., & Coppersmith, K. J. (1984). Fault behavior and characteris-
 1137 tic earthquakes: Examples from the Wasatch and San Andreas Fault Zones.
 1138 *Journal of Geophysical Research*, *89*, 5681–5698. Retrieved from [http://](http://doi.wiley.com/10.1029/JB089iB07p05681)
 1139 doi.wiley.com/10.1029/JB089iB07p05681 doi: 10.1029/JB089iB07p05681
- 1140 Segall, P., & Pollard, D. D. (1983). Nucleation and growth of strike slip faults in
 1141 granite. *Journal of Geophysical Research: Solid Earth (1978–2012)*, *88*, 555–
 1142 568.
- 1143 Seidl, M. A., Dietrich, W. E., & Kirchner, J. W. (1994, jul). Longitudinal Profile
 1144 Development into Bedrock: An Analysis of Hawaiian Channels. *The Journal of*
 1145 *Geology*, *102*(4), 457–474. Retrieved from <https://doi.org/10.1086/629686>
 1146 doi: 10.1086/629686
- 1147 Slemmons, D. B. (1957). Geological effects of the Dixie Valley-Fairview Peak
 1148 Nevada, Earthquakes of December 16, 1954. *Bulletin of the Seismological*
 1149 *Society of America*, *47*(1934), 353–357.
- 1150 Smekalin, O., Chipizubov, A., & Imaev, V. (2010). Paleoearthquakes in the Baikal
 1151 region: Methods and results of timing. *Geotectonics*, *44*(2), 158–175. Re-
 1152 trieved from <http://dx.doi.org/10.1134/S0016852110020056> doi: 10.1134/
 1153 [s0016852110020056](http://dx.doi.org/10.1134/S0016852110020056)
- 1154 Smith, T. R., & Bretherton, F. P. (1972). Stability and the Conservation of Mass in
 1155 Drainage Basin Evolution. *Water Resources Research*, *8*(6), 1506–1529.
- 1156 Stamps, D., Saria, E., & Kreemer, C. (2018). A geodetic strain rate model for the
 1157 east african rift system. *Scientific reports*, *8*(1), 732.
- 1158 Stein, S., & Liu, M. (2009). Long aftershock sequences within continents and impli-
 1159 cations for earthquake hazard assessment. *Nature*, *462*(7269), 87–89.
- 1160 Stirling, M., Goded, T., Berryman, K., & Litchfield, N. (2013). Selection of earth-
 1161 quake scaling relationships for seismic-hazard analysis. *Bulletin of the Seismo-*
 1162 *logical Society of America*, *103*(6), 2993–3011. doi: 10.1785/0120130052
- 1163 Sun, C., Wan, T., Xie, X., Shen, X., & Liang, K. (2016). Knickpoint series
 1164 of gullies along the Luoyunshan Piedmont and its relation with fault ac-
 1165 tivity since late Pleistocene. *Geomorphology*, *268*, 266–274. Retrieved
 1166 from <http://dx.doi.org/10.1016/j.geomorph.2016.06.026> doi:

- 1167 10.1016/j.geomorph.2016.06.026
- 1168 Swan, F. H., Schwartz, D. P., & Cluff, L. S. (1980). Recurrence of Moderate to
1169 Large Magnitude Earthquakes Produced by Surface Faulting on the Wasatch
1170 Fault Zone, Utah. *Bulletin of the Seismological Society of America*, *70*(5),
1171 1431–1462.
- 1172 Villamor, P., & Berryman, K. (2001). A late quaternary extension rate in
1173 the Taupo Volcanic Zone, New Zealand, derived from fault slip data.
1174 *New Zealand Journal of Geology and Geophysics*, *44*(2), 243–269. doi:
1175 10.1080/00288306.2001.9514937
- 1176 Vittori, E., Delvaux, D., & Kervyn, F. (1997, sep). Kanda fault: A major seismo-
1177 genic element west of the Rukwa Rift (Tanzania, East Africa). *Journal of Geo-*
1178 *dynamics*, *24*, 139–153. Retrieved from [http://linkinghub.elsevier.com/](http://linkinghub.elsevier.com/retrieve/pii/S0264370796000385)
1179 [retrieve/pii/S0264370796000385](http://linkinghub.elsevier.com/retrieve/pii/S0264370796000385) doi: 10.1016/S0264-3707(96)00038-5
- 1180 Walker, R. T., Wegmann, K. W., Bayasgalan, A., Carson, R. J., Elliott, J., Fox, M.,
1181 ... Wright, E. (2015). The Egiin Davaa prehistoric rupture, central Mongolia:
1182 a large magnitude normal faulting earthquake on a reactivated fault with little
1183 cumulative slip located in a slowly deforming intraplate setting. *Seismicity,*
1184 *Fault Rupture and Earthquake Hazards in Slowly Deforming Regions*, *432*,
1185 187–212. Retrieved from [http://sp.lyellcollection.org/content/early/](http://sp.lyellcollection.org/content/early/2015/11/17/SP432.4.abstract)
1186 [2015/11/17/SP432.4.abstract](http://sp.lyellcollection.org/content/early/2015/11/17/SP432.4.abstract) doi: 10.1144/SP432.4
- 1187 Wallace, R. E. (1977). Profiles and ages of young fault scarps, north-central Nevada.
1188 *Geological Society of America Bulletin*, *88*, 1267–1281.
- 1189 Wallace, R. E. (1980). Degradation of the Hebgen Lake fault scarps of 1959. *Geol-*
1190 *ogy*, *8*(5), 225–229. doi: 10.1130/0091-7613(1980)8(225:DOTHLF)2.0.CO
- 1191 Wallace, R. E. (1984). *Fault scarps formed during the earthquakes of October 2,*
1192 *1915, in Pleasant Valley, Nevada, and some tectonic implications.* US Govern-
1193 ment Printing Office.
- 1194 Walshaw, R. D. (1965). The geology of the Ncheu-Balaka area. *Bulletin of the Geo-*
1195 *logical Survey, Malawi*, *19*(96).
- 1196 Wei, Z., Bi, L., Xu, Y., & He, H. (2015). Evaluating knickpoint recession along an
1197 active fault for paleoseismological analysis: The Huoshan Piedmont, Eastern
1198 China. *Geomorphology*, *235*, 63–76. Retrieved from [http://dx.doi.org/](http://dx.doi.org/10.1016/j.geomorph.2015.01.013)
1199 [10.1016/j.geomorph.2015.01.013](http://dx.doi.org/10.1016/j.geomorph.2015.01.013) doi: 10.1016/j.geomorph.2015.01.013
- 1200 Wells, D., & Coppersmith, K. (1994). New empirical relationships among magni-
1201 tude, rupture length, rupture width, rupture area, and surface displacement.
1202 *Bulletin of the Seismological Society of America*, *84*(4), 974–1002. Retrieved
1203 from <http://bssa.geoscienceworld.org/content/84/4/974.short>
- 1204 Whipple, K. X., & Tucker, G. E. (1999). Dynamics of the stream-power river in-
1205 cision model: Implications for height limits of mountain ranges, landscape
1206 response timescales, and research needs. *Journal of Geophysical Research:*
1207 *Solid Earth*, *104*(B8), 17661–17674.
- 1208 Whittaker, A. C., Attal, M., Cowie, P. A., Tucker, G. E., & Roberts, G. (2008).
1209 Decoding temporal and spatial patterns of fault uplift using transient
1210 river long profiles. *Geomorphology*, *100*(3-4), 506–526. doi: 10.1016/
1211 [j.geomorph.2008.01.018](http://dx.doi.org/10.1016/j.geomorph.2008.01.018)
- 1212 Whittaker, A. C., Cowie, P. A., Attal, M., Tucker, G. E., & Roberts, G. P. (2007a).
1213 Bedrock channel adjustment to tectonic forcing: Implications for predicting
1214 river incision rates. *Geology*, *35*(2), 103–106. doi: 10.1130/G23106A.1
- 1215 Whittaker, A. C., Cowie, P. A., Attal, M., Tucker, G. E., & Roberts, G. P. (2007b).
1216 Contrasting transient and steady-state rivers crossing active normal faults:
1217 New field observations from the central apennines, Italy. *Basin Research*,
1218 *19*(4), 529–556. doi: 10.1111/j.1365-2117.2007.00337.x
- 1219 Willemse, E. J. M., & Pollard, D. D. (1998). On the orientation and patterns of
1220 wing cracks and solution surfaces at the tips of a sliding flaw or fault. *Journal*
1221 *of Geophysical Research: Solid Earth*, *103*, 2427–2438. Retrieved from <http://>

- doi.wiley.com/10.1029/97JB01587 doi: 10.1029/97JB01587
- 1222 Williams, J. N., Fagereng, Å., Wedmore, L. N., Biggs, J., Mphepo, F., Dulanya, Z.,
 1223 ... Blenkinsop, T. (2019). How do variably striking faults reactivate during
 1224 rifting? insights from southern malawi. *Geochemistry, Geophysics, Geosystems*,
 1225 *20*(7), 3588–3607. Retrieved from [https://agupubs.onlinelibrary.wiley](https://agupubs.onlinelibrary.wiley.com/doi/abs/10.1029/2019GC008219)
 1226 [.com/doi/abs/10.1029/2019GC008219](https://agupubs.onlinelibrary.wiley.com/doi/abs/10.1029/2019GC008219) doi: 10.1029/2019GC008219
 1227
- 1228 Wohl, E. E. (1993). Bedrock channel incision along Piccaninny Creek, Australia.
 1229 *The Journal of Geology*, *101*(6), 749–761.
- 1230 Wu, D., & Bruhn, R. L. (1994). Geometry and kinematics of active normal faults,
 1231 South Oquirrh Mountains, Utah: implication for fault growth. *Journal of*
 1232 *Structural Geology*, *16*(8), 1061–1075. doi: 10.1016/0191-8141(94)90052-3
- 1233 Xu, Y., He, H., Deng, Q., Allen, M. B., Sun, H., & Bi, L. (2018). The CE
 1234 1303 Hongdong Earthquake and the Huoshan Piedmont Fault, Shanxi
 1235 Graben: Implications for Magnitude Limits of Normal Fault Earthquakes.
 1236 *Journal of Geophysical Research: Solid Earth*, *123*(4), 3098–3121. doi:
 1237 10.1002/2017JB014928
- 1238 Yang, J., Guo, Z., & Cao, J. (1985). Investigation on the Holocene activities of the
 1239 Helan mountain piedmont fault by use of geomorphological method. *Seismol-*
 1240 *ogy and Geology (in Chinese with English abstract)*, *7*(4), 23–31.
- 1241 Yu, L., Porwal, A., Holden, E.-J., & Dentith, M. C. (2011). Suppression of
 1242 vegetation in multispectral remote sensing images. *International Jour-*
 1243 *nal of Remote Sensing*, *32*(22), 7343–7357. Retrieved from [https://](https://www.tandfonline.com/doi/full/10.1080/01431161.2010.523726)
 1244 www.tandfonline.com/doi/full/10.1080/01431161.2010.523726 doi:
 1245 10.1080/01431161.2010.523726
- 1246 Zhang, P., Slemmons, D. B., & Mao, F. (1991). Geometric pattern, rupture termina-
 1247 tion and fault segmentation of the Dixie Valley-Pleasant Valley active normal
 1248 fault system, Nevada, U.S.A. *Journal of Structural Geology*, *13*(2), 165–176.
 1249 Retrieved from [http://www.sciencedirect.com/science/article/pii/](http://www.sciencedirect.com/science/article/pii/019181419190064P)
 1250 [019181419190064P](http://www.sciencedirect.com/science/article/pii/019181419190064P)
- 1251 Zielke, O., Klinger, Y., & Arrowsmith, J. R. (2015). Fault slip and earthquake re-
 1252 currence along strike-slip faults - Contributions of high-resolution geomorphic
 1253 data. *Tectonophysics*, *638*(1), 43–62. Retrieved from [http://dx.doi.org/](http://dx.doi.org/10.1016/j.tecto.2014.11.004)
 1254 [10.1016/j.tecto.2014.11.004](http://dx.doi.org/10.1016/j.tecto.2014.11.004) doi: 10.1016/j.tecto.2014.11.004
- 1255 Zielke, O., & Strecker, M. R. (2009). Recurrence of large earthquakes in mag-
 1256 matic continental rifts: Insights from a paleoseismic study along the Laikipia-
 1257 Marmaret fault, Subukia Valley, Kenya rift. *Bulletin of the Seismological*
 1258 *Society of America*, *99*(1), 61–70. doi: 10.1785/0120080015